(Received 18 September 2025, Accepted 22 October 2025, Scheduled 23 December 2025)

Decoupled-Mode Plasmonic Metamaterials for Ultra-High-Q Tailored Mid-Infrared Extraordinary Optical Transmission

Roy Avrahamy[1, *], Mark Auslender[1], Moshe Zohar[2], Amiel A. Ishaaya[1], and Benjamin Milgrom[3]

[1] *School of Electrical and Computer Engineering, Ben-Gurion University of the Negev, P.O.B. 653, Beer-Sheva 8410501, Israel*
[2] *Electrical and Electronics Engineering Department, Shamoon College of Engineering, P.O.B. 950, Beer Sheva 8410802, Israel*
[3] *School of Electrical Engineering, Jerusalem College of Technology, P.O.B. 16031, Jerusalem 9372115, Israel*

ABSTRACT: Plasmonic designs for mid-infrared extraordinary optical transmission (EOT), a direct route to tailored filtering with broadband out-of-band rejection, have long been constrained by a fundamental trade-off between high transmission efficiency and narrow linewidths, a challenge rooted in the material properties of noble metals. Here, we theoretically propose and numerically demonstrate a versatile design paradigm that resolves this challenge by functionally decoupling the tasks of light coupling and resonant filtering. Our approach uses a dual-stacked noble metal-dielectric grating architecture to surpass the intrinsic limitations of single-layer structures. This paradigm provides the flexibility to engineer devices for ultra-high spectral selectivity and transmission efficiency. We demonstrate this with distinct designs: one at 10 μm with a quality factor (Q-factor) > 2000 and $> 91\%$ transmission; a high-Q design at 4 μm and $> 80\%$ transmission; and a high-efficiency design at 4 μm with $> 92\%$ transmission over a uniquely broad spectral-angular range. These generic designs produce solitary, narrow EOT peaks originating from a "triple-coupling" mechanism that mitigates reflection and absorption losses, with symmetry-broken configurations capable of exceeding Q-factors of 16,000 while maintaining a peak transmission efficiency $> 60\%$. Crucially, these compact two-layer designs exhibit exceptional robustness against fabrication variations, offering a broadly applicable route to ultra-compact, low-cost infrared components, enabling advanced architectures such as angular sensing, spectro-polarimetric imaging, and isotope-resolved gas diagnostics.

1. INTRODUCTION

The fundamental-vibrations resonances of many molecules, and peaks of thermal radiation emission from many objects with temperatures between $-70°$ and $+1100°$C, are located in the $3\ \mu\text{m} \leq \lambda \leq 15\ \mu\text{m}$ wavelength range. This part of infrared (IR) is subdivided due to the atmospheric windows into mid-wave IR (MWIR) and long-wave IR (LWIR) ones, and these are associated with hotter and colder objects, such as rocket engines and biological species, respectively. As a result, optical sensing and filtering in the MWIR and LWIR are highly demanded in the fields of health, security and defense, geoscience, and communication; and plasmonics has been claimed [1, 2] perspective for these important applications.

1.1. The Challenge of High-Performance Plasmonics in the Mid-Infrared

Translating the success of plasmonics from the visible and near-infrared (NIR) [3, 4] to the mid-infrared has proven to be a formidable challenge, requiring a fundamental distinction in the physical mechanism. While the intrinsic surface plasmon frequency (ω_{sp}) of noble metals lies in the ultraviolet/visible range, their utility in the mid-infrared is defined by their behavior as near-perfect conductors with minimal ohmic loss. In this "Drude" regime, the resonances are not intrinsic material transitions but rather geometric resonances arising from structural confinement. A key consequence is that the supported surface plasmon polaritons (SPPs) are less tightly confined to the metal-dielectric interface and possess macroscopic propagation lengths. Consequently, plasmonic devices in this regime often face a debilitating trade-off: designs that achieve narrow spectral linewidths, which are essential for high-resolution sensing, typically suffer from low transmission or coupling efficiency due to high reflection or absorption losses. Conversely, designs that achieve high transmission often exhibit broad resonances, limiting their spectral selectivity (or sensitivity). The common benchmark for the resonance spectral linewidth is the quality factor: Q-factor (or Q for brevity), defined by the full width at half maximum (FWHM) of the resonance peak as $Q = \lambda_{\text{res}}/\text{FWHM}$.

Extraordinary optical transmission (EOT) through periodically sub-λ holed/stripped thin metal films [5–8] has emerged as a promising avenue for creating compact optical filters and sensors. Yet, even within the EOT framework, the fundamental mid-infrared plasmon trade-off persists. For single-layer gratings, the narrow slits required to excite high-Q SPP-driven resonances suffer from a significant impedance mismatch with free-space radiation, leading to strong reflection and absorption, and consequently, poor transmission. In contrast, wider slits that support high-transmission standing-wave modes typically produce broad, low-Q spectral features, rendering them unsuitable for high-sensitivity applications. This persistent challenge has hindered the development of integrated, high-performance plasmonic components for the mid-infrared.

* Corresponding author: Roy Avrahamy (roiav@post.bgu.ac.il).

1.2. State-of-the-Art in High-Q Metamaterials

A significant research effort has focused on overcoming the intrinsic losses of plasmonic systems to achieve ultra-high-Q resonances. A major breakthrough has been the exploitation of collective diffractive coupling in periodic nanoparticle arrays, giving rise to Surface Lattice Resonances (SLRs) [9, 10]. By suppressing radiative damping through the coherent interaction of all nanoparticles in the lattice, SLRs have enabled plasmonic metasurfaces with record-breaking experimental Q-factors. Notably, [10] demonstrated a plasmonic metasurface with a Q-factor of approximately 2340 in the telecommunication C-band ($\sim$1.55 μm). Such ultra-high-Q resonances are accompanied by intense local field enhancements, making them highly attractive for nonlinear optics and sensing.

Most high-Q plasmonic designs in the mid-IR operate in reflection or absorption/emission modes, such as Tamm plasmon absorbers [11] and emitters [12], or quasi-bound states in the continuum (BIC) metasurfaces [13]. Recent theoretical works have pushed predicted Q-factors far beyond current experimental realizations. For example, plasmonic quasi-BIC metasurfaces have been modeled with $Q \sim 938$ in the mid-IR [13], and nonlocal coupling strategies suggest $Q > 1000$ [14]. While these approaches achieve narrow linewidths, they do not provide high-Q transmission through an opaque metal film.

A significant body of research has explored alternative plasmonic materials with more favorable properties in the infrared. These include highly-doped semiconductors (e.g., InAs) [15], transparent conducting oxides (e.g., ITO), transition metal nitrides (e.g., TiN), and graphene [16], which offer the ability to tune the plasma frequency into the mid-IR, providing a more moderate dielectric response compared to noble metals [17, 18]. While the development of alternative materials is a vital and promising research direction, the approach taken here, using a conventional noble metal within a novel architecture, has several advantages. The most prominent one being fabrication maturity and reliability. Silver is a cornerstone material in nanofabrication, with well-established and highly reliable deposition and patterning processes such as sputtering and electron-beam lithography. In contrast, many alternative materials require more specialized and complex fabrication methods. For example, high-quality, heavily-doped semiconductors often necessitate molecular beam epitaxy (MBE), a sophisticated and less common technique. By adhering to a standard material, the designs leverage decades of process knowledge, making the path to realization more direct and predictable.

Another powerful approach is the use of all-dielectric metasurfaces [19, 20], which are free from metallic losses and can achieve exceptionally high Q-factors by leveraging mechanisms like guided-mode resonances (GMRs) [21] and, most notably, BICs [22–24]. Indeed, recent advances in fabrication and design, have pushed the experimental Q-factors of all-dielectric *reflection-mode* GMR and BIC metasurfaces to over a million in the near Vis. (779 nm) [21] and 100,000 in the NIR [24], respectively.

However, to replicate the EOT function — narrowband transmission through an otherwise opaque screen, all-dielectric platforms typically require a complex multilayer stack, typically a Distributed Bragg Reflector (DBR), involving the precise deposition of numerous alternating high- and low-index layers to achieve the necessary broadband rejection. This complexity makes them architecturally less compact than their plasmonic counterparts. While all-dielectric metasurfaces can achieve exceptionally high Q-factors, often by leveraging BICs, these resonant features are typically designed on top of, or within, these complex foundational mirror structures. In contrast, our dual-grating architecture delivers ultra-high-Q resonances in EOT mode with near-unity transmission efficiency, addressing a long-standing challenge in both mid-IR plasmonics and all-dielectric platforms.

1.3. A Dual-Grating Approach for Decoupled Mode Engineering

This survey of the current landscape reveals a clear and critical gap: there is no established plasmonic design paradigm that can simultaneously deliver ultra-high Q-factors (> 2000), near-unity transmission efficiency ($> 90\%$), and high angular sensitivity in the MWIR and LWIR spectral bands. In this work, we address this critical gap by proposing and investigating a novel metamaterial design concept based on a vertically stacked dual-grating architecture. We hypothesize that the inherent performance limitations of single-layer EOT structures can be overcome by physically separating and optimizing the functions of light in-coupling and resonant transmission. Our design consists of two metallic gratings with highly disparate aperture ratios: a wide-slit grating that acts as an efficient antenna to couple incident radiation to surface modes, and a narrow-slit grating that supports a high-Q resonant cavity mode.

By engineering the near-field coupling and spectral alignment of these distinct modes through careful optimization of the geometric parameters, we achieve a synergistic coupling between these two distinct functionalities. This paper reports on the design and performance of this Optimized Generic Design (OGD), which yields highly enhanced EOT peaks with unprecedented Q-factors and near-perfect transmission, solitary in the MWIR and LWIR bands. We numerically demonstrate designs operating around 4 μm and 10 μm that exhibit exceptional angular sensitivity while maintaining stable peak transmission. We then delve into a detailed near-field analysis to elucidate the underlying physical mechanism, which we identify as a "triple-coupling" process involving SPPs, localized corner-field radiators, and a confined standing-wave mode. Finally, we validate the practical viability of our designs through a comprehensive fabrication tolerance analysis, which provides compelling evidence for our proposed physical model of decoupled mode engineering. This work presents a new and robust pathway for realizing ultra-compact, high-performance plasmonic devices that can overcome long-standing challenges in mid-infrared photonics.

1.4. Theoretical Background

The physical mechanism behind EOT is not straightforward. Rather, it is a sophisticated interplay of several mechanisms, clearly described for 1D-periodic slit arrays in [25], see also the comprehensive reviews [26–30]. In detail, an incident elec-

tromagnetic (EM) wave which, for a 1D grating, is necessarily TM polarized, (magnetic field vector **H** is along the slits' direction), excites a surface mode (SM) at the film-superstrate interface, from which an EM field portion is tunnelled through the slits and excites another SM at the film-substrate interface that may cause forward/backward EM radiation to the far-field. Depending on λ, and the ratios such as aperture ratio a/Λ (AR), a/λ, and h/λ, where Λ and h are the grating pitch and depth, respectively, and a is the slit width, the transfer is aided by either evanescent or Fabry-Perot-like standing-wave (SW) modes. SM at each interface is composed of an SP mode and a quasi-cylindrical waves (QCW) modal mixture, and relative weights of the SP and QCW components were assessed with a simplified model supported by a rigorous EM analysis [27, 31, 32]. More complicated EOT scenarios are realized for 2D periodic hole arrays, for which the incidence polarization is not restricted [26–30].

The EOT effect is propelled or inhibited, depending on coupling or decoupling, respectively, between the dominant components of SMs at the opposite interfaces. In the visible and NIR ranges, where in the complex refractive index (RI) of the metal, $n_m + ik_m$, n_m/k_m is not too small, the inhibition is frequently due to SP resonant absorption [33]. In MWIR and LWIR, where $n_m/k_m \ll 1$, and towards the perfect conductor state, where this ratio vanishes, the SP is no longer resonant, although persists with a decreased weight [27, 31, 32]. In these ranges, the EOT inhibition is mostly due to reflection, although a dominant absorption regime may be designed.

First, there is the sudden drop in transmittance, which corresponds to the Rayleigh anomaly (RA), the geometric threshold where the m-th diffraction order passes off at a grazing angle of $\pm 90°$. The Rayleigh wavelength corresponds to

$$\lambda_R^{\pm} = \frac{\Lambda}{m}\left(n_{\text{diff}} \pm n_{\text{inc}} \sin\theta_{\text{inc}}\right), \tag{1}$$

where Λ is the grating period (pitch), m the integer diffraction order ($m = 1, 2, 3\ldots$), θ_{inc} the angle of incidence, and n_{inc} and n_{diff} are the refractive index of the incidence medium and the medium into which the order diffracts, respectively. The second phenomenon, occurring at a slightly longer wavelength (lower energy) than the Rayleigh anomaly for the same order m, is the Wood anomaly (WA). This is the physical resonance where the light couples into an SPP mode:

$$\lambda_{\text{Wood}}^{\pm} = \frac{\Lambda}{m}\left(\Re\left\{n_{\text{eff}}(\lambda)\right\} \pm n_{\text{inc}} \sin\theta_{\text{inc}}\right). \tag{2}$$

For a metal-dielectric interface, replace the wavelength dependent effective refractive index, n_{eff}, with the SPP dispersion relation:

$$\lambda_{\text{Wood}}^{\pm} = \frac{\Lambda}{m}\left(\Re\left\{\sqrt{\frac{\varepsilon_m(\lambda)\varepsilon_d(\lambda)}{\varepsilon_m(\lambda)+\varepsilon_d(\lambda)}}\right\} \pm n_{\text{inc}} \sin\theta_{\text{inc}}\right). \tag{3}$$

where $\varepsilon_m(\lambda)$ and $\varepsilon_d(\lambda)$ are the complex permittivities of the metal and dielectric, respectively, and $\Re\{\,\}$ denotes the real part. The SPP can be launched on either the superstrate or substrate if they are different.

The mathematical mechanism behind EOT is a constructive synergy between SMs propagating at the patterned film interface and the EM Bloch eigenmodes (BEMs) inside the film, which are matched at the interfaces. Retaining just one BEM is the essence of the model in [25, 27, 31, 32]. At the QCW-SP coupling, the transmittance spectrum $T(\lambda)$ is narrow around the EOT peak and exhibits high sensitivity, which unfortunately is accompanied by a severe peak amplitude (T_p) deterioration at the cost of increasing absorption [33]. In the QCW-SP decoupling regime supported by SWs in the slits, the EOT peak is wide, fairly insensitive to moderate changes in RI of the relevant ambient and/or angular positioning, and highly robust with regards to T_p [5, 34].

2. RESULTS

2.1. Design

We extensively examined numerous generalized designs with structural variations, such as with different numbers of smooth/grating layers. The study included both specific simulations and general optimization flows, and hence we achieved an optimized generic design (OGD), as shown in Fig. 1. The structure consists of a dual-stacked grating system fabricated on a low-refractive-index polymer or dielectric substrate. The "back" grating (layer 1, facing the substrate) is a metal film with wide slits, corresponding to a low metal filling fraction and a large aperture ratio of $a_1/\Lambda = 0.5$. The "front" grating (layer 2, facing the ambient medium, typically air) is a metal film with narrow slits, corresponding to a high metal filling fraction and a small aperture ratio of $a_2/\Lambda = 0.1$. Both gratings share a common period, Λ. The slits in both gratings and the space between them are filled with the same dielectric material as the substrate. This stacked configuration, with its engineered asymmetry in aperture ratios, is the cornerstone

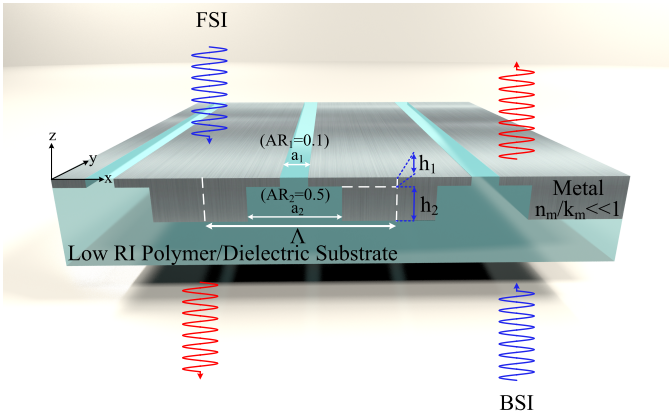

FIGURE 1. Schematic of the proposed dual-grating EOT structure for mid- and long-wave IR. The design consists of two vertically stacked metallic gratings on a low-index substrate: a front grating with a narrow slit array (10% aperture ratio) and a back grating with a wide slit array (50% aperture ratio). Both gratings share the same period Λ, and the slits and interlayer gap are filled with the same dielectric/polymer material as the substrate. F/BSI — front/back side illumination. For a detailed 2D cross-sectional schematic with labeled geometric parameters, see Supplementary Fig. S23.

of the design, intended to decouple the functions of light collection and resonant filtering.

Subject to the substrate constraint of the OGD, SPs propagating either along the air-metal (AM) or the dielectric-metal (DM) interface can be launched by the gratings with $\lambda_{SP}^{(AM)} \gtrsim \Lambda$ or $\lambda_{SP}^{(DM)} \gtrsim \Lambda n_d$, respectively. The lower bounds of the SP wavelengths are the Rayleigh wavelengths of the appropriate interface. For small-θ back-side illumination (BSI) at $\lambda_{SP}^{(AM)} < \lambda < \lambda_{SP}^{(DM)}$, only 0-order transmission takes place, whereas extra ± 1 diffraction-orders may be reflected back to the substrate. At λ moderately below $\lambda_{SP}^{(AM)}$, further diffraction orders may emerge in the transmission, whereas at $\lambda > \lambda_{SP}^{(DM)}$ the radiation is reflected and transmitted only by the 0-order waves. Upon mutual transmittance-to-reflectance interchange, the above speculation fully applies to small-θ front-side illumination (FSI). Thus, SP at the AM-interface seems not to be an appropriate candidate for propelling the 0-order EOT, a conjecture that was verified using numerous optimization runs. Simultaneously, the DM-interface SP excitation wavelength is within the diffractionless spectral regime, and it is this SP that, with the OGD optimal parameters, proves to match and successfully provide the superior EOT performance requirements.

The optimization strategy proceeded as follows: First, the grating period Λ was chosen to be slightly smaller than the Rayleigh anomaly threshold at the dielectric-metal (DM) interface, i.e., $\Lambda \lesssim \lambda_0/n_d$. This condition is known to be critical for exciting SPP-mediated EOT. A compromise was made, as moving Λ closer to the threshold increases the Q-factor at the cost of slightly lower peak transmittance T_p. With the aperture ratios fixed at 50% and 10% and Λ selected, the automated optimization routine was then used to find the optimal thicknesses of the back and front gratings, h_1 and h_2, respectively, with the objective function set to maximize the peak transmittance T_p at the central design wavelength (CDW) λ_0 under normal incidence. This approach consistently yielded designs with the highest achievable Q-factors as well.

To validate the design concept and achieve optimal performance, we employed a comprehensive numerical modeling and optimization framework, cross-validating our results with two distinct computational methods. The primary design and optimization were conducted using an in-house, custom-developed implementation of the Rigorous Coupled-Wave Analysis (RCWA) method. The final optimized designs obtained from the RCWA framework were subsequently verified using the Wave Optics Module of the commercial finite element method (FEM) software, COMSOL Multiphysics®. The results from the FEM simulations showed good agreement with the RCWA predictions, providing high confidence in the simulated performance, see details in Section 4 and comparison in Supplementary Fig. S9.

Following the optimization procedure, we investigated the performance of three distinct OGD structures: two designed for the MWIR at $\lambda_0 = 4\,\mu$m (dubbed M_1 and M_2) and one for the LWIR at $\lambda_0 = 10\,\mu$m (dubbed L_1). The M_1 and L_1 designs were optimized for high sensitivity and selectivity under normal BSI, while the M_2 design was optimized for maximum peak transmittance under normal FSI. The final geometric parameters for these structures are detailed in Table 1.

TABLE 1. Optimized geometric parameters of the three plasmonic metamaterial designs. The refractive index n_d of the dielectric material (PDMS for M_1, M_2; CaF_2 for L_1) is given at the central design wavelength, λ_0.

Parameter	M_1	M_2	L_1
Illumination	BSI	FSI	BSI
λ_0	4.0 μm	4.0 μm	10.0 μm
Λ	2.8429 μm	2.8392 μm	7.6923 μm
h_1 (back grating)	0.2208 μm	0.3051 μm	0.7037 μm
h_2 (front grating)	0.1267 μm	0.0427 μm	0.2006 μm
$n_d\,(\lambda_0)$	1.407	1.407	1.3

The choice of materials is guided by the target spectral range and performance requirements. For operation in the MWIR and LWIR, the metal must exhibit a strong plasmonic response, characterized by the complex RI $n_m + ik_m$ with the above-noted extinction domination. Silver (Ag) offers superior performance when dissipative losses can be effectively managed, which is a central achievement of this design. The optical constants for Ag were taken from [35]. The dielectric substrate and filling material must be transparent in the target band with a relatively low RI n_d, typically $1 < n_d < 2.5$. For the designs presented here, in the MWIR (around 4 μm) we use PDMS as the low-index fill/substrate ($n_d \approx 1.40$), which is transparent across the near-to-mid IR. If a *lower-index* and low-loss replacement for PDMS is desired at 4 μm, we recommend *magnesium fluoride* (MgF_2), which provides $n \approx 1.36$–1.38 with negligible k at 4 μm [36, 37]; *calcium fluoride* (CaF_2) with $n \approx 1.39$ at 4 μm is also suitable [38]. As an optional polymeric route to reduce the index further, *Teflon AF* ($n \approx 1.29$–1.31) can be considered when thermal/vacuum requirements permit, noting the processing and stability caveats [39, 40]. These substitutions preserve the optical function while reducing Fresnel reflections and maintaining low absorption at $\sim 4\,\mu$m.

For the LWIR spectral range, material selection is critical due to the onset of multiphonon absorption. To address this, we defined and analyzed two distinct design configurations tailored to the transparency windows of fluoride substrates:

1. Deep LWIR Design (L_1): Targeted at $\lambda_0 = 10\,\mu$m, this design serves as a benchmark for high-EOT-Q filtering. While CaF_2 ($n_d \approx 1.3$ [38]) is often used in the IR, and its extinction coefficient rises to $k \approx 3\times10^{-4}$ at 10 μm [41, 42]. Supplementary simulations revealed that using CaF_2 for L_1 deteriorates the performance (see Supplementary Fig. S13). Consequently, for this specific band, we identify Barium Fluoride (BaF_2) as the requisite substrate material ($k \approx 1 \times 10^{-5}$ [43, 44]), which recovers the high efficiencies.

2. Optimal CaF_2 Design (C_1): To demonstrate the performance ceiling within the optimal transparency window of CaF_2, we optimized a supplementary design centered at 8.2 μm ($h_1 = 0.517\,\mu$m, $h_2 = 0.254\,\mu$m, $\Lambda = 6.094\,\mu$m). Simulations utilized vendor-measured wavelength-dependent optical constants ($k \approx 3.3 \times 10^{-5}$ at 8.2 μm [41]).

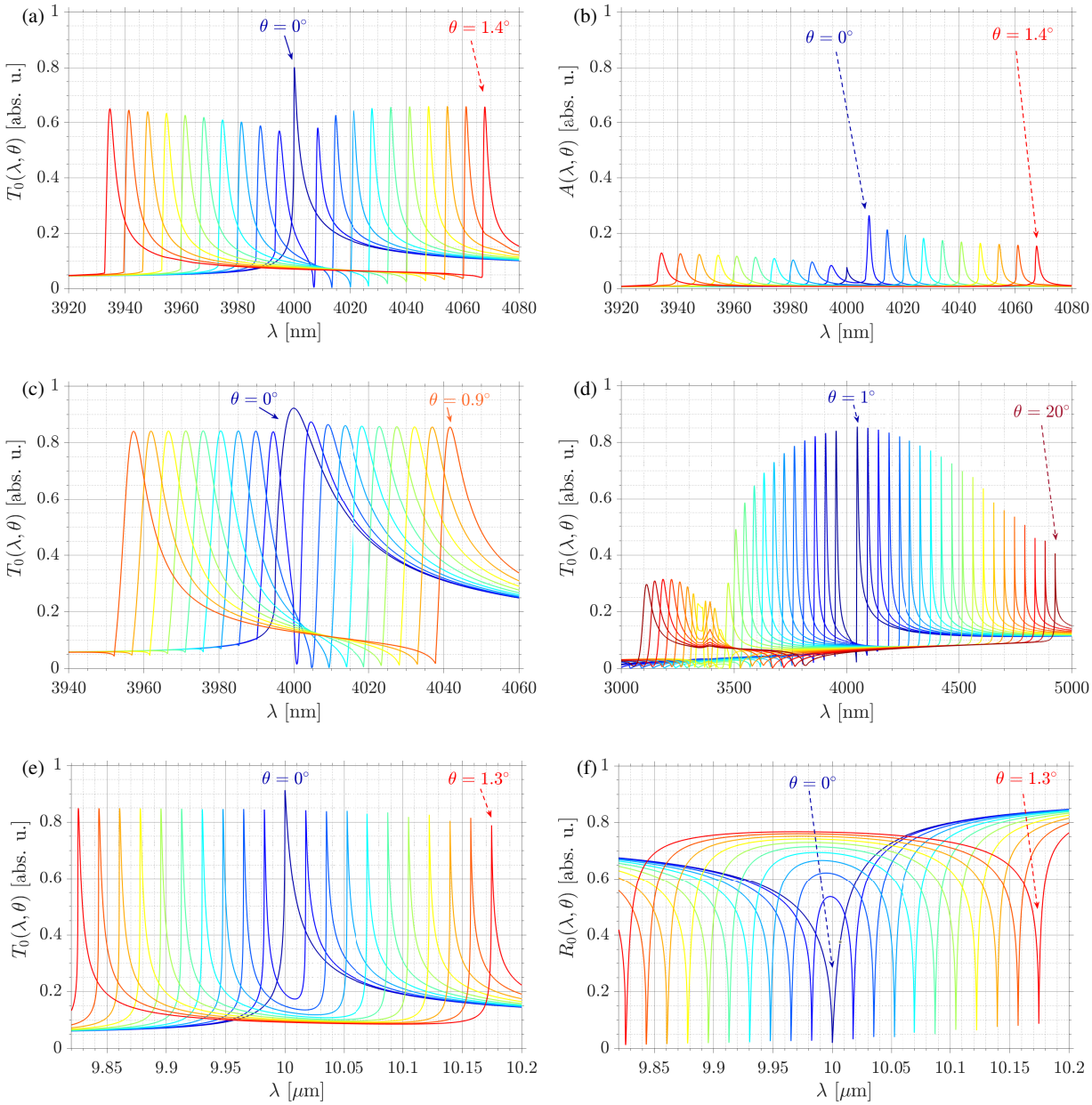

FIGURE 2. The spectral-angular optical responses from the designed meta-materials. M_1 under BSI and at 3.92 µm $\leq \lambda \leq$ 4.08 µm, $0° \leq \theta \leq 1.4°$: (a) transmittance, (b) absorptance; transmittance via M_2 under FSI at (c) 3.94 µm $\leq \lambda \leq$ 4.06 µm, $0° \leq \theta \leq 0.9°$, and (d) 3 µm $\leq \lambda \leq$ 5 µm, $1° \leq \theta \leq 20°$; L_1 under BSI and at 9.82 µm $\leq \lambda \leq$ 10.2 µm, $0° \leq \theta \leq 1.3°$: (e) transmittance, (f) reflectance. The θ sampling intervals correspond to Supplementary Table S1.

To extend performance deeper into the LWIR ($>$ 10 µm), *cryolite* (Na_3AlF_6, $n \approx 1.32$–1.35 in thin films) that extends to $\sim$ 14–16 µm, with negligible k in this band is recommended. As an *optional* polymer alternative offering an even lower refractive index, *Teflon AF* (amorphous perfluoropolymer) provides $n \simeq 1.29$–1.31 and manufacturer-reported high transmission from the infrared through the ultraviolet [39, 40]. We caution that (i) specific mid-IR vibrational bands can occur in fluoropolymers, and (ii) processing/environmental constraints apply (spin-coated films; use temperature $\lesssim 285°$C; decomposition $> 360°$C) [40]. When used within these limits, Teflon AF can serve as a low-index over or inter-layer for LWIR stacks, but our primary recommendations for 10–12 µm remain the inorganic fluorides BaF_2 and cryolite due to their established LWIR performance [45, 46].

2.2. Far-Field Spectral-Angular Performance

A selection of the simulated spectral-angular optical responses for the three designs is presented in Fig. 2. Comprehensive performance metrics are plotted in Fig. 3 and highlighted for convenience in Supplementary Table S1. For compatibility with experimental instrumentation, all reported angles, θ, are free-space angles in both F/BSI.

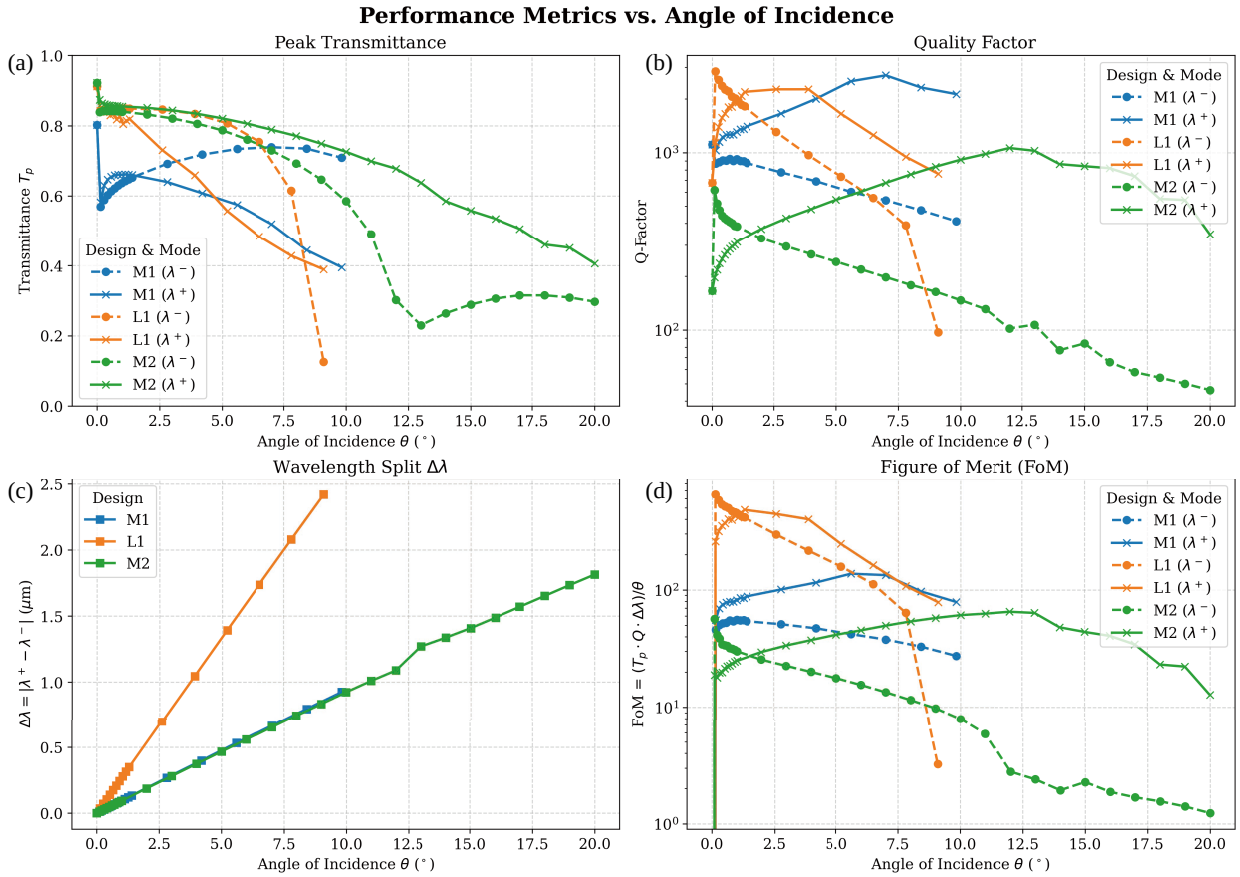

FIGURE 3. Comprehensive performance metrics of the optimized EOT designs as a function of the angle of incidence (θ). The plots compare the performance of the M_1 (blue), L_1 (orange), and M_2 (green) designs for both the lower (λ^-, dashed lines, 'o' markers) and upper (λ^+, solid lines, 'x' markers) resonant modes. (a) Peak transmittance (T_p) for each mode. (b) Quality factor (Q-factor) plotted on a logarithmic scale to accommodate the wide range of values. (c) The spectral split between the two resonant modes, $\Delta\lambda = |\lambda^+ - \lambda^-|$. (d) The calculated Figure of Merit: FOM $= (T_p \cdot Q \cdot \Delta\lambda)/\theta$, also on a logarithmic scale, illustrating the angular sensing potential of each design. Note that the inflection points observed in the dispersion curves (panels a, c) correspond to the spectral overlap of the onset diffraction order with λ^-.

A striking feature across all designs is the presence of an extremely sharp, high-amplitude transmission peak at the design wavelength for normal incidence ($\theta = 0°$). Crucially, these peaks are solitary; our simulations confirm that there are no other significant zero-order transmission peaks throughout the entire MWIR and LWIR bands, a critical feature for practical applications like filtering where side-band rejection is paramount. To validate the rejection performance, we provide extended broadband spectra in Supplementary Figs. S16–S21. These analyses (log-scale transmission, absorption/reflection balance, and diffraction order efficiency) confirm that the out-of-band energy is predominantly reflected rather than absorbed, and that parasitic diffraction orders remain negligible in the spectral-spatial sensing window.

For any non-normal incidence angle ($\theta > 0°$), the single peak splits into two distinct resonances, at wavelengths $\lambda_0^-(\theta)$ and $\lambda_0^+(\theta)$, located to the left and right of the original peak, respectively. The high $T_0(\lambda, \theta)$ peak amplitudes, particularly given the small 10% aperture ratio of the front grating, and against other single grating configuration, are indicative of a highly efficient, tailored, EOT process. The spectral positions, $\lambda_0^-(\theta)$ and $\lambda_0^+(\theta)$, and separations, $\Delta\lambda$ of the split EOT peaks, highlighted in Fig. 3(c), follow Eq. (3) (WA) with good accuracy. Bearing in mind the RIs of the materials (and thus n_{eff}) typically decreases slightly (normal dispersion) or changes due to the SPP dispersion curve flattening. Thus, the λ^+ (λ^-) peak doesn't move exactly as far to the right (left) as the non-dispersive formula predicts. This phenomenon is quantified by the Group Index (n_g) of the surface mode. The actual sensitivity is scaled by the group index:

$$\Delta\lambda_{\text{real}} \approx \frac{2\Lambda \sin\theta}{n_g} \tag{4}$$

where $n_g = n_{\text{eff}} - \lambda \frac{dn_{\text{eff}}}{d\lambda}$.

WA is typical of the EOT propelled by the above-mentioned SP excitation [26, 28–30]. Thus, we reasonably conclude that the EOT phenomenon, in our case, is due to SPs at the substrate (DM) interface, while high transmission due to SPs at the superstrate (AM) interface is suppressed at the cost of high reflection (not shown).

Figures 2(a) and 2(b) show $T_0(\lambda, \theta)$ and $A(\lambda, \theta)$ of M_1, respectively, for $0° \leq \theta \leq 1.4°$. In Fig. 2(a), $T_p(0°) \gtrsim 80\%$, from which one obtains $Q = 1111$; correspondingly, Fig. 2(b) shows that there is a complementary low sharp peak of $A(\lambda, 0°)$

with $A_p(0^\circ) \gtrsim 7.5\%$. As seen in Fig. 2(a), the amplitudes of the split peaks, $T_p^-(\theta)$ and $T_p^+(\theta)$, are close but not equal. At the lowest investigated θ, $T_p^{\mp}(\theta)$ instantly drop down to be slightly less than 60%, but with further increase of θ steadily rise to overshoot this level. The reasons for the drops below T_p are different for $T_p^-(\theta)$ and $T_p^+(\theta)$. Namely, for the back-to-substrate reflection, the grating, in addition to the ever-possible zero-order wave, may support at $\lambda \lesssim \lambda_0$ both $+1$ and -1st order diffracted waves, whereas at $\lambda > \lambda_0$ only a -1st order one may be supported. Let $R_1(\lambda, \theta)$ be the reflection efficiencies of the diffracted waves. Our analysis reveals that a concordant change in the $A(\lambda_0^+(\theta), \theta) = A_p^+(\theta)$ peaks, see Fig. 2(b), and in the $R_0(\lambda_0^+(\theta), \theta)$ dips (not shown) has the effect of decreasing $T_p^+(\theta)$ at $\theta = 0.1^\circ$ and maintains its small changes at higher θ. Yet, not only $A(\lambda_0^-(\theta), \theta) = A_p^-(\theta)$ and $R_0(\lambda_0^-(\theta), \theta)$ contribute to the initial downward jump of $T_p^-(\theta)$, and further keep it slowly varying, but also $R_{-1}(\lambda_0^-(\theta), \theta)$. This explains why the maxima of the $T_p^{\pm}(\theta)$ peaks show very low deterioration at $\theta > 0.1^\circ$, despite notable asymmetry between angular-split spectral maxima left, $A_p^-(\theta)$, and right, $A_p^+(\theta)$, to λ_0 — as seen in Fig. 2(b).

Figures 2(c) and 2(d) show the $T_0(\lambda, \theta)$ curves of M_2 under FSI at small and higher incidence angles ($0^\circ \le \theta \le 0.9^\circ$ and $1^\circ \le \theta \le 20^\circ$), respectively. As seen in Figs. 2(c), 2(d), 3(a), and 3(b) and in accordance with its design targets, the M_2 shows the highest $T_p(0^\circ) \gtrsim 92\%$ and, relative to the other two designs, lowest $Q(0^\circ) = 166$. In Fig. 2(c), the amplitudes $T_p^{\pm}(\theta)$ remain almost constant vs. θ, although with the step $\Delta\theta = 0.1^\circ$, the peaks spectrally overlap; for better resolution $\Delta\theta = 0.2^\circ$ should be used. Fig. 2(d), which embeds the spectral range of Fig. 2(c), reveals quite peculiar spectral behavior for $\theta \ge 1^\circ$. Namely, at $3.5\,\mu\text{m} < \lambda < 5\,\mu\text{m}$ a comb of the split peaks appears with a clearly observable regular envelope that is asymmetric with respect to λ_0. In particular, at increasing θ the amplitudes $T_p^+(\theta)$ prove more stable than $T_p^-(\theta)$, with maximal $Q^+(12^\circ) = 1061$, and show satisfactorily high performance up to $\lambda = 4.926\,\mu\text{m}$ with $T_p^+(20^\circ) > 40\%$ and $Q^+(20^\circ) = 347$ (see Fig. 2(d) and Figs. 3(a)–(b)). A sharp jump of $Q^-(\theta)$ at the first angle step from $\theta = 0^\circ$ to $\theta = 0.1^\circ$ is followed by a further monotonic decrease of both $Q^-(\theta)$ and $T_p^-(\theta)$. $T_p^{\mp}(\theta) > 50\%$ is maintained up to $\theta \simeq 11^\circ$, which remains over a $\gtrsim 1\,\mu\text{m}$ wide spectral range at $3.508\,\mu\text{m} < \lambda < 4.516\,\mu\text{m}$. Note that similar spectral-angular transmittance peak combs are found for two other structures, but over a narrower angular range (Figs. 3(a)–(b)). An interplay effect of the angular-split SPs at the AM and DM interfaces is evident in the largely weakened and increased Q-factor (still maintaining EOT), and the $T_0(\lambda, \theta)$ peaks observed in Fig. 2(d) at $3\,\mu\text{m} \le \lambda \le 3.5\,\mu\text{m}$, $\theta \ge 12^\circ$, within the diffraction range. Since the design parameters of M_2 were optimized for EOT over Q, they provide a greater and exceptional spectral sensitivity range that covers almost the entire MWIR range.

Figures 2(e) and 2(f) show the $T_0(\lambda, \theta)$ and $R_0(\lambda, \theta)$ curves, respectively, of L_1 under BSI in the same spectral-angular range $9.82\,\mu\text{m} \le \lambda \le 10.2\,\mu\text{m}$, $0^\circ \le \theta \le 1.3^\circ$. As seen in Supplementary Table S1 and Figs. 3(a)–(b), the designed EOT peak $T_p(0^\circ) = T_0(\lambda_0, 0^\circ) \gtrsim 91\%$ is only 1% inferior to that of M_2, and notably surpasses that of M_1. Moreover, for L_1 the split peak decrease upon the increase of θ to 0.1° is notably smaller than for M_1, as can be seen from comparing Fig. 2(a) to Fig. 2(e). Remarkably, see Supplementary Table S1 and Figs. 3(a)–(b), $T_p^-(\theta)$ is nearly constant at $0.13^\circ \le \theta \le 2.6^\circ$, oscillating within $\pm 0.5\%$, and slowly monotonically decreases in total by $\sim 0.9\%$ over the next range, $2.6^\circ \le \theta \le 6.5^\circ$. Similarly, $T_p^+(\theta)$ oscillates in the same range, but on a twice larger scale, and decreases fast by $\sim 30\%$ over the next θ range. In the oscillation range $Q^-(\theta)$ also oscillates, attaining values up to 2852, while in the monotonically decreasing range it drops down to much lower values. Concurrently, $Q^+(\theta)$, remaining high and quite stable over a wider range of $0.13^\circ \le \theta \le 6.5^\circ$, shows a lower scale of oscillation and a lower maximum. The $R(\lambda, \theta)$ dips in Fig. 2(f) are nearly complementary to, and as sharp as, the $T(\lambda, \theta)$ peaks in Fig. 2(e). Moreover, these dips are remarkably stable and low at $\lambda \le 10\,\mu\text{m}$, and only slowly increase above $10\,\mu\text{m}$. Apart from the quantitative differences, the $A(\lambda, \theta)$ spectrum of L_1 (not shown) is similar to that of M_1 and, *vice versa*, the $R(\lambda, \theta)$ spectrum of M_1 (not shown) is similar to that of L_1. Yet, since the $T(\lambda, \theta)$ peaks (Fig. 2(e)) and $R(\lambda, \theta)$ dips (Fig. 2(f)) are most predominantly high and low, respectively, (which is not the case for M_1), L_1 may perform angular sensing well, both in transmission and in reflection modes. As shown in Supplementary Fig. S14, Design C_1 shows comparably, to the L_1, robust high-Q performance with $T_p > 80\%$.

Finally, the Figure of Merit: FOM $= (T_p \cdot Q \cdot \Delta\lambda)/\theta$ in Fig. 3(d) highlights the LWIR design's superior angular sensitivity at small tilts, while the MWIR design (M_2) offers a broad operational range with stable FOM across wide angles. These trends underscore the versatility of the dual-grating architecture: by adjusting geometric parameters, one can prioritize ultra-narrowband filtering or wide-angle tunability for application-specific requirements. This is evidently due to the surplus synergy of the two gratings. Indeed, as discussed below, the single slit-grating meta-structure with a narrow slit that is the same as that of the front grating in the OGDs of the considered structure, does not perform in this way. This is further confirmed in visualization of the EM fields (**E**, **H**) and power flux density (Poynting vector **S**).

To underscore the necessity of the dual-grating architecture, a comparison is made with that of a well-studied single-grating EOT metamaterial. To this end, as is elaborated in [25], and verified by simulations with our materials, a distinction is made between symmetric and asymmetric scenarios. For the air-dielectric substrate (asymmetric) case, such as the OGDs investigated herein, with similar irradiation conditions as those for EOT-M$_{1,2}$, $-\lambda_0 = 4\,\mu\text{m} \simeq \lambda_{\text{SP}}^{(\text{DM})}$, and a design constrained at Λ not less than that of EOT-M$_2$ ($2.8392\,\mu\text{m}$ and $a_1/\Lambda \le 0.5$, a value of $T_p(0^\circ) \approx 33.3\%$ can be achieved, at best, with $\Lambda = 2.8392\,\mu\text{m}$, $a_1/\Lambda = 0.5$ and $h_1 = 2.1\,\mu\text{m}$. Interestingly, while this is the highest attainable $T_p(0^\circ)$ for any $a_1/\Lambda \le 0.5$, examining the spectrum for a wide range of h_1 with a fixed wide slit of $a_1/\Lambda = 0.5$ reveals that, $\lambda_{\text{SP}}^{(\text{DM})} \lesssim \lambda_0$ is typically a local minimum point of $T_0(\lambda, 0^\circ)$, appearing in between two wide, low-Q, transmission peaks. Moreover, given λ_0, $T_0(\lambda_0, 0^\circ)$ tends to zero at $\Lambda \to \lambda_0/n_{\text{d}}$. These two numerical findings indicate a negative role of SPs in the EOT buildup [33].

In addition, we investigate the performance of optimized single narrow-slit gratings (SNSGs) with a 10% aperture ratio, detailed in Supplementary Fig. S1. Two cases are considered. In Case 1, the grating period is set well below the Rayleigh limit ($\Lambda < \lambda_0/n_d$). This design achieves high transmission ($\sim$80%) but produces a very broad, low-Q resonance characteristic of a Fabry-Pérot mode, which is also insensitive to the angle of incidence. In Case 2, the period is set near the Rayleigh limit ($\Lambda \approx \lambda_0/n_d$) to excite an SPP-mediated resonance. This yields a narrower spectral feature, but the peak transmittance plummets to just 22% due to a severe impedance mismatch, leading to high reflection ($\sim$47%) and absorption ($\sim$31%).

For a single-grating structure in the symmetric case, e.g., periodically slit membrane in air, even with ARs as large as 50%, $\lambda_{\mathrm{SP}}^{(\mathrm{AM})} \simeq \Lambda$ can be the point of a local maximum of $T_0(\lambda, 0^\circ)$. In this case, $T_{\mathrm{p}}(0^\circ)$ at optimal $h_1 = 2.2538$ μm reaches $\approx 81.8\%$ with a high $Q(0^\circ) > 1000$. As discussed in the Introduction section, and proved in [25, 47], this sharp peak is due to the resonant coupling between the SP modes at similar AM interfaces, which are degenerate in energy. An additional, much wider, EOT peak appears visibly to the right of λ_0 in the $T_0(\lambda, 0^\circ)$ spectrum, simulated after the optimization. Since this peak strongly resembles the peaks that have been attributed to the resonant SW modes effect in the analysis of [25, 47] for another structure of the same type, and discussed above, we reasonably draw the same conclusion in this case. As the slits are made more narrow, the SP-derived EOT peak rapidly deteriorates because of complementary absorption/reflection losses, whereas that due to the SW resonance withstands the narrowing, despite displaying red shifts. Oblique incidence has quite a similar effect: while the wide peak withstands it, the narrow one vanishes just at a very small value of θ.

Examining the dual-grating OGD EOT structures investigated in this study, and referring to the properties of the single-gratings reported in the literature and discussed above, we may state that stacking one more grating with a very different AR onto the metamaterial may enable the highest EOT performance of the former, combining the best aspects and suppressing the performance of the latter found in both symmetric and asymmetric cases, and with both wide and narrow slits. It appears that the low Q-factor peaks typical of the effects of the SW modes with the wide slits are inhibited by concurrent narrow-to-wide gratings interlocking and decoupling due to the asymmetry, whereas high absorption/reflection losses typical of the effect of the SP modes with the narrow slits are reduced in favor of far-field radiating transmission via the wide slits. In this context, it seems very probable that the comb of very narrow, sharp peaks and its 1.5 μm wide spectral envelope (seen in Fig. 2(d)) are the result of an overlap of the θ-insensitive SW excitation-derived wide EOT band that peaks well to the right of $\lambda_{\mathrm{SP}}^{(\mathrm{AM})}$; further, the peaks due to SPs excited at the DM interface with sharp spectral positions around $\lambda_0 \simeq \lambda_{\mathrm{SP}}^{(\mathrm{DM})}$ strongly depend on θ, as seen in Eq. (3). It is worth emphasizing that all of the above single slit-grating EOT configurations, however optimized, fail to perform as efficiently as our OGDs, which maintain high amplitude and Q-factor EOT spectral peaks over very wide θ and λ ranges (see Fig. 3).

To demonstrate the flexibility of the proposed architecture, we investigated both BSI and FSI. Due to the metallic losses, the system is non-Hermitian, and strict Lorentz reciprocity does not guarantee identical bidirectional responses for all observables [48–50]. In fact, while the transmission spectrum remains reciprocal (i.e., $T_{\mathrm{BSI}}(\lambda, \theta) = T_{\mathrm{FSI}}(\lambda, \theta)$ for corresponding wavevectors), reflection and absorption generally differ when flipping the illumination direction due to asymmetric field penetration and loss distribution. This behavior is consistent with prior analyses of lossy metasurfaces and asymmetric gratings [48, 49]. Unlike active or time-modulated platforms that break Lorentz reciprocity [51, 52], our structure remains reciprocal in transmission but exhibits asymmetric reflection and absorption due to loss and geometric asymmetry along the z-axis (stacking direction). The ability to operate efficiently under both BSI and FSI highlights the design's versatility for integration in diverse optical layouts.

2.3. Unveiling the Triple-Coupling Enhancement Mechanism

In Fig. 4, we display color maps of $|\mathbf{E}|^2 = |E_x|^2 + |E_z|^2$ and $|H_y|^2$ for normal incidence and CDW ($\theta = 0^\circ, \lambda = \lambda_0$) over an x-z area, where $0 \le x \le \Lambda$ and z is over a depth range that covers the structure plus some parts of its vicinity; $\langle S_z \rangle_x$ and the cumulative absortptance $\mathcal{A}(z)$, obtained by summing its differentials in z, are plotted together vs. z in the same range. In addition, the normal incidence transmittance and reflectance at CDW can accurately be assessed with $\langle S_z \rangle_x$ values given by

$$\langle \mathbf{S} \rangle_x = \frac{1}{\Lambda} \int_0^{\Lambda} \mathbf{S}\,(x, z)\, dx, \tag{5}$$

at the corresponding ambient-structure interfaces.

As established with the SNSG benchmark, a single narrow slit fails because energy coupled to the DM-interface SPP is inefficiently funneled through the slit and is instead mostly reflected or absorbed. The dual-grating structure solves this problem through a three-stage process we term "triple-coupling":

- SPP Excitation (In-Coupling): For BSI (M_1, L_1), incident light efficiently excites a propagating SPP mode on the DM interface of the wide-slit back grating. This layer acts as an effective antenna, overcoming the impedance mismatch that hinders direct excitation of narrow slits.
- Localized Corner-Field Radiation (Energy Funneling): The near-field plots (Figs. 4(a), (c), (e)) reveal intense electric field enhancement ($|\mathbf{E}|^2$) localized at the sharp metal corners of the wide back-grating slits. These corners act as highly efficient secondary radiators, collecting energy from the propagating SPP and funneling it directly towards the aperture of the front grating.
- Standing-Wave Resonance (High-Q Filtering): The energy injected from the back grating excites a high-Q, standing-wave-like mode within the narrow front-grating slit. This mode is characterized by a strong, uniform electric field, similar to a parallel-plate capacitor, which then radiates efficiently into the far-field.

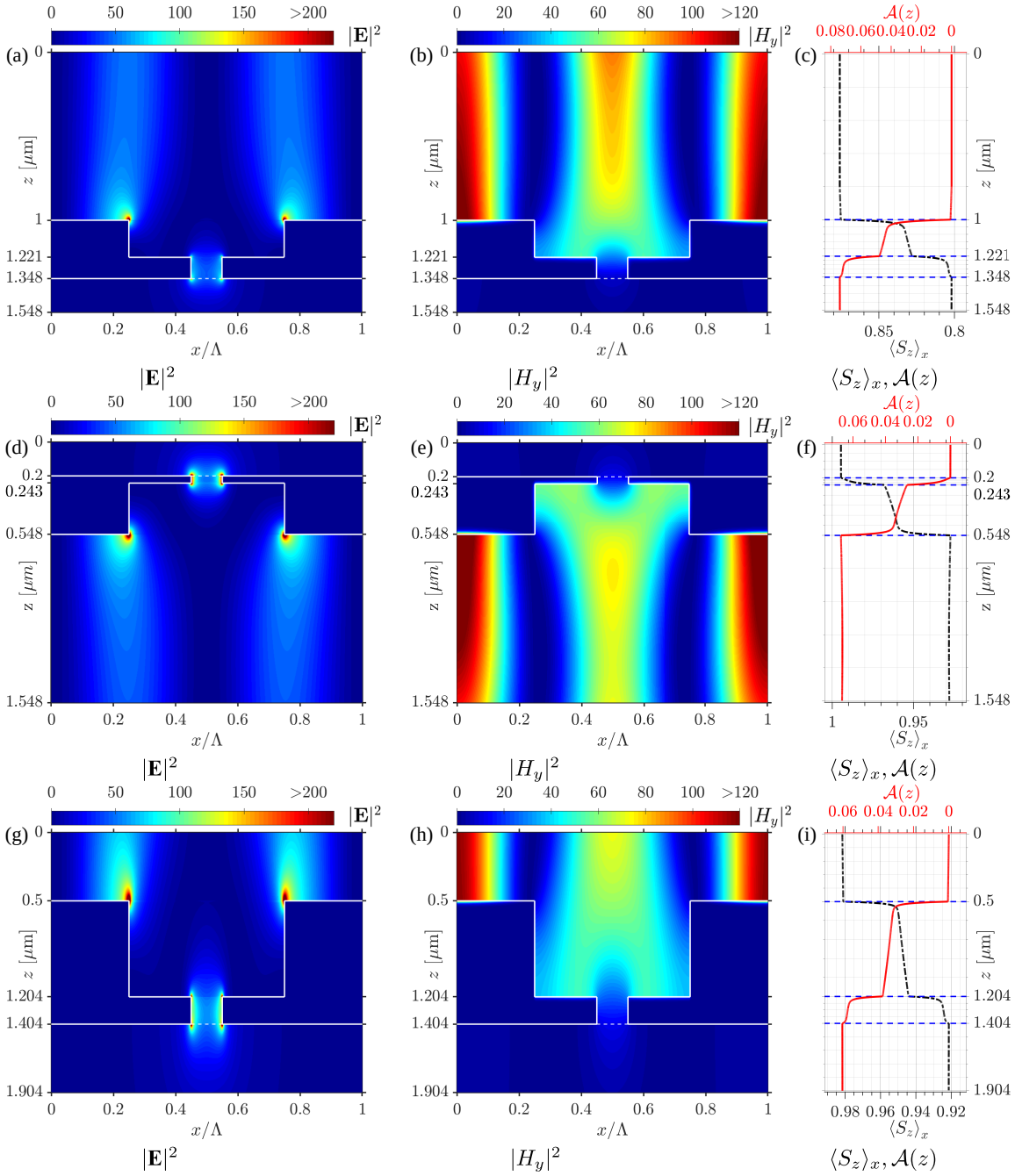

FIGURE 4. Near-field analysis at resonance ($\theta = 0°, \lambda = \lambda_0$) for designs (a)–(c) M_1, (d)–(f) M_2, and (g)–(i) L_1. The left and center columns show squared amplitudes of the electric ($|\mathbf{E}|^2$) and magnetic ($|H_y|^2$) fields, respectively. The right column plots the period-averaged Poynting vector component $\langle S_z\rangle_x$ (black dash-dot line, bottom axis) and cumulative absorptance $\mathcal{A}(z)$ (red solid line, top axis) versus depth z. The plots reveal intense field localization at the back-grating corners, which is central to the triple-coupling mechanism.

This mechanism effectively decouples the functions: the back grating handles efficient energy collection, while the front grating provides high-Q resonant filtering. To visually confirm this energy pathway, we performed a detailed Poynting vector analysis. Supplementary Fig. S10 presents the vector quiver plots for BSI, showing power flux lines converging at the back-grating corners. Furthermore, to validate the mechanism's reciprocity, we calculated the energy streamlines under FSI conditions (Supplementary Fig. S11). These streamlines explicitly reveal energy being captured by the front slit and funneled back to converge at the same corners. This bidirectional confirmation identifies the corners as critical radiative elements facilitating coupling between the high-Q cavity and the propagating surface plasmons. It is pertinent to classify the resonant mechanism in the context of itinerant versus localized modes [53, 54]. While the optical fields are confined within the sub-wavelength slits and at the corners, this localization is distinct from the quasi-static Localized Surface Plasmon Resonances (LSPRs) where frequency is pinned to the plasma frequency ($\omega \propto \omega_p$). Instead, the confinement here represents

a *geometric* cavity mode formed by gap-plasmons (a Fabry-Perot-like standing wave). The macroscopic optical response is thus governed by the coupling between these geometrically localized modes and the itinerant (running) SPPs propagating along the metal-dielectric interfaces.

To quantify the underlying physics of the "triple-coupling" mechanism, we applied Temporal Coupled-Mode Theory (TCMT) to decompose the total quality factor (Q_{tot}) into its radiative (Q_{rad}) and absorptive (Q_{abs}) components. Instead of relying solely on spectral fitting, we calculated these factors directly from the electromagnetic field integrals. For the L_1 design at the transmission peak ($\lambda = 10.00\,\mu\text{m}$), we extracted $Q_{abs} \approx 4.8 \times 10^4$ and $Q_{rad} \approx 3.4 \times 10^3$. Furthermore, at the intrinsic physical resonance frequency ($\lambda \approx 9.999\,\mu\text{m}$), where the stored energy is maximal, the absorptive quality factor reaches an exceptional value of $Q_{abs} \approx 2.1 \times 10^5$. This ratio ($Q_{abs} \gg Q_{rad}$) quantitatively confirms that the resonance is dominated by radiative coupling to the external environment rather than ohmic dissipation. This suppression of intrinsic loss is a key factor enabling the simultaneous achievement of high-Q and near-unity transmission. It is noteworthy that the intrinsic Q-values derived from energy dynamics are significantly higher than those extracted from the spectral linewidth (FWHM); this difference arises from the asymmetric Fano lineshape of the dual-grating interference, which spectrally broadens the transmission profile despite the high internal mode confinement. The full analysis of the energy dynamics for all designs is detailed in Supplementary Fig. S18.

The mechanism behind the remarkable *angular* performance of OGDs discussed in Subsection 2.2 is analyzed here using the field and **S** visualizations in Fig. 5. To this end, we choose the M_1 structure and $\theta = 0.5°$. At $\theta > 0°$ the right and left propagating SPs are non-degenerate in energy since $\lambda_0^+(\theta) \neq \lambda_0^-(\theta)$, and they have opposite predominant propagation directions. Following the above analysis for normal incidence, it is not surprising that the fields inside the substrate and back grating are highly affected by varying θ. Most notable are the highly localized peak of $|\mathbf{E}|^2$ at $z = 0.421\,\mu\text{m}$, which is magnified either at the left corner, $x = 0.45\Lambda$, for $\lambda_0^-(\theta)$ or at the right one, $x = 0.55$, for $\lambda_0^+(\theta)$, and, correspondingly, the peaked plasmonic $|H_y|^2$ patterns located either at $x = 0.25\Lambda$ or at $x = 0.75\Lambda$. The low amplitudes of $|H_y|^2$ within the lateral area around the narrow slit $0.45 < x/\Lambda < 0.55$ appear as domes that begin inside the back grating at $z = 0.421\,\mu\text{m}$ and stretch up with a diagonal tilt towards $z = 0\,\mu\text{m}$. These domes, which are a visualization of the θ tilt, are straightened inside the front grating due to the SW mechanism, and inside the air there is no clear evidence of the tilt. As reported in the literature and noted above, an SW-based EOT has a very low tilt sensitivity, and the field patterns are similar to those shown here for $0.421\,\mu\text{m} < z < 0.748\,\mu\text{m}$. The spectral-angular EOT performance at $\theta > 0°$ of the alternative plasmonic configuration with a single grating in a symmetric ambiance, fails due to plasmons launched at the metamaterial interfaces with input and output mediums, which annihilate the effect of each other inside the opening. As discussed in Subsection 2.2, the back and front gratings of OGDs, separately placed in a non-symmetric configuration show poor EOT angular performance. The constructive SW-SP mode synergies of OGDs provide the record broadband EOT angular performance envelope with excellent IR plasmonic sensing capabilities and particularly ultrahigh Q.

The quiver plot visualization of **S** with $\theta = 0.7°$ at $\lambda_0^-(\theta)$ and $\lambda_0^+(\theta)$ in Figs. 5(e) and (f), respectively, provide additional details regarding the OGD angular performance mechanism. Since the field magnitudes are shown in Figs. 5(a), (b), (c), and (d), for clarity, the magnitude of the quiver arrows is normalized separately for each of the three lateral sections dividing the sub-figures (e), (f). Thus, comparison should be in terms of the flow direction, and the magnitudes should be treated in accordance. The flow directions at $\lambda_0^-(\theta)$ and $\lambda_0^+(\theta)$ display remarkable mirror-like symmetry in all sections. Inside the substrate, the **S** flow is predominantly lateral and, similarly to the normal incidence case (but less strongly), bends towards and concentrates at the corners. In these cases, the stronger corner transfers, while the weaker reverses the flow, a tendency which is also found inside the back grating, where the lateral flow still prevails, propelled by SP flow at the DM interface. Inside the front grating, however, the lateral flow changes to a vertical one. Spatially, the alteration originates in the dome-like patterns of $|H_y|^2$ above and below the narrow slit and proceeds into it. As seen in Figs. 5(c), (d), oblique incidence stretches the domes, and this phenomenon is assisted by an enhanced corner. Following the direction alteration inside the front grating, the flow towards the ambient air is predominantly vertical and concentrated near the front-grating slits; this, again, is similar to the case of SW-supported EOT via the single-slit grating structure.

2.4. Robustness and Practical Viability: A Fabrication Tolerance Analysis

To assess the practical viability of the proposed designs, a comprehensive fabrication tolerance analysis was conducted. We systematically evaluated the sensitivity of the key performance metrics: λ_0, Q factor, and T_p to variations in the critical geometric parameters. The thicknesses (h_1, h_2) and the widths of the slits (a_1, a_2) were varied by $\pm 5\%$ from their nominal values, while the impact of corner rounding, a common fabrication artifact, was modeled by varying the corner radii $(r_{1,2,3})$ of a perfectly sharp corner up to 100 nm. A summary of this analysis is presented in Fig. 6, with detailed plots available in the Supplementary Figs. S2–S8.

The analysis reveals a powerful and counterintuitive insight that strongly validates our proposed physical model of decoupled functions. Across all three designs, the device performance is critically more sensitive to the wide, back-grating dimensions (a_1, h_1) but is remarkably robust to variations in the narrow, front-slit dimensions (a_2, h_2). For instance, in the L_1 (M_1) design, a 5% negative deviation in a_1 causes the Q-factor to decrease by $\sim$15% (27%), whereas a similar change in a_2 results in a negligible variation of less than 1.3% (8.9). This disparity provides compelling evidence that the back grating acts as a precision-tuned coupler or antenna, where the geometry must be exact to efficiently match the incident radiation to the propagating SPP mode. In contrast, the front grating functions

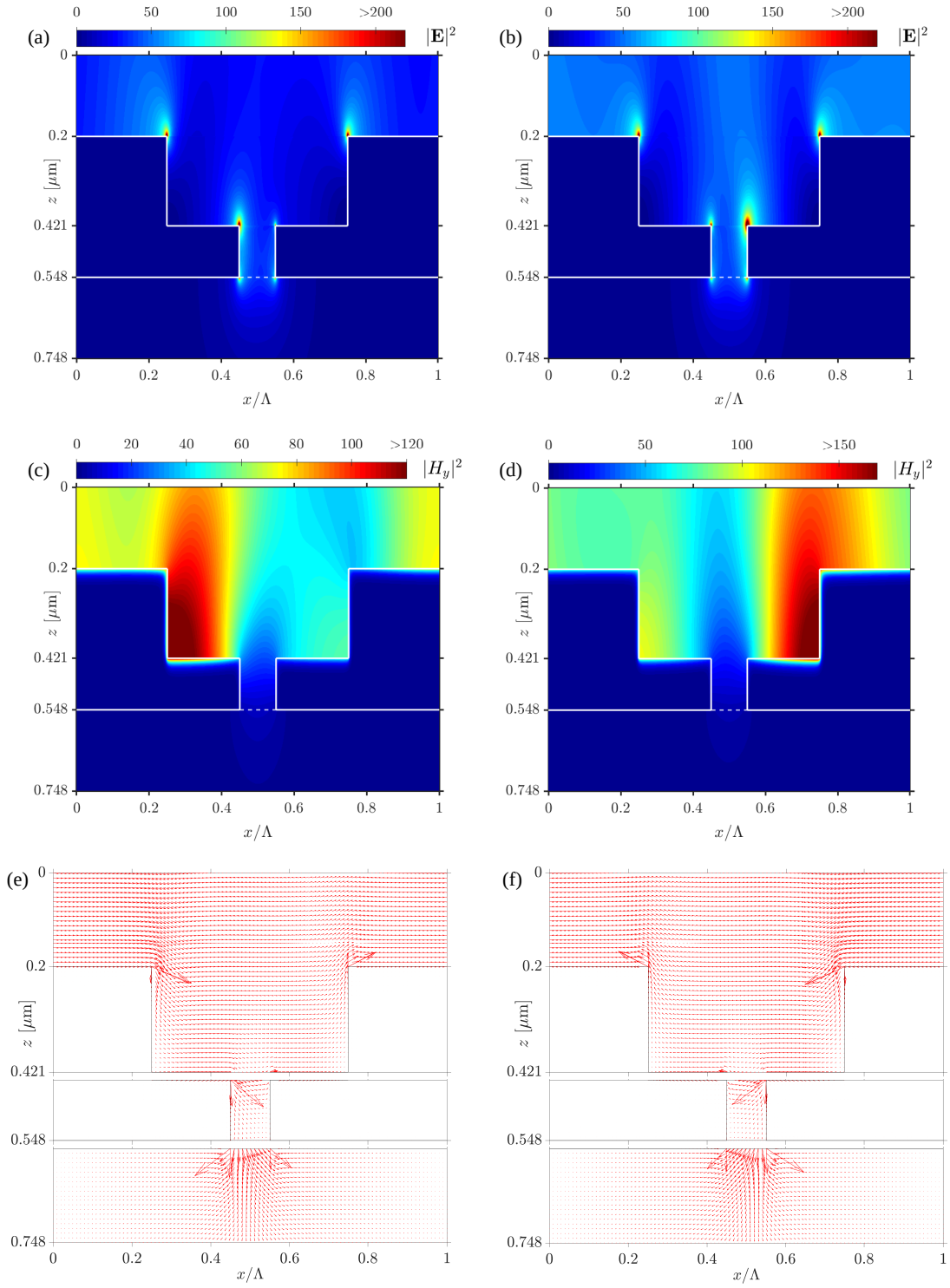

FIGURE 5. Color maps of (a), (b) $|\mathbf{E}|^2$ and (c), (d) $|H_y|^2$, and (e), (f) **S** quiver plots for M_1 at slightly oblique incidence under $\theta = 0.7^\circ$ at two wavelengths corresponding to the split angular EOT peaks: (a), (c), (e) $\lambda = \lambda_0^-(0.7^\circ) = 3.968$ µm; and (b), (d), (f) $\lambda = \lambda_0^+(0.7^\circ) = 4.0346$ µm. The quiver plot sub-figures (e) and (f) are virtually subdivided into three lateral sections: a part of (i) dielectric/polymer + back grating; (ii) front grating; and (iii) ambient air. For the best visibility, the **S** arrows presentation is separate per each section and independent of the others; $|\mathbf{S}|$ is largest in the upper section, and regularly decreases down to the lower one, as can be inferred from the $|\mathbf{E}|^2$ and $|H_y|^2$ color maps.

as a robust standing-wave resonator, whose performance is not critically dependent on the precise aperture dimension once the energy has been efficiently injected.

This physical picture is further supported by the analysis of the corner radii (Supplementary Fig. S4). To rigorously differentiate between correlative and causative structural factors, we performed a site-specific corner rounding analysis under FSI.

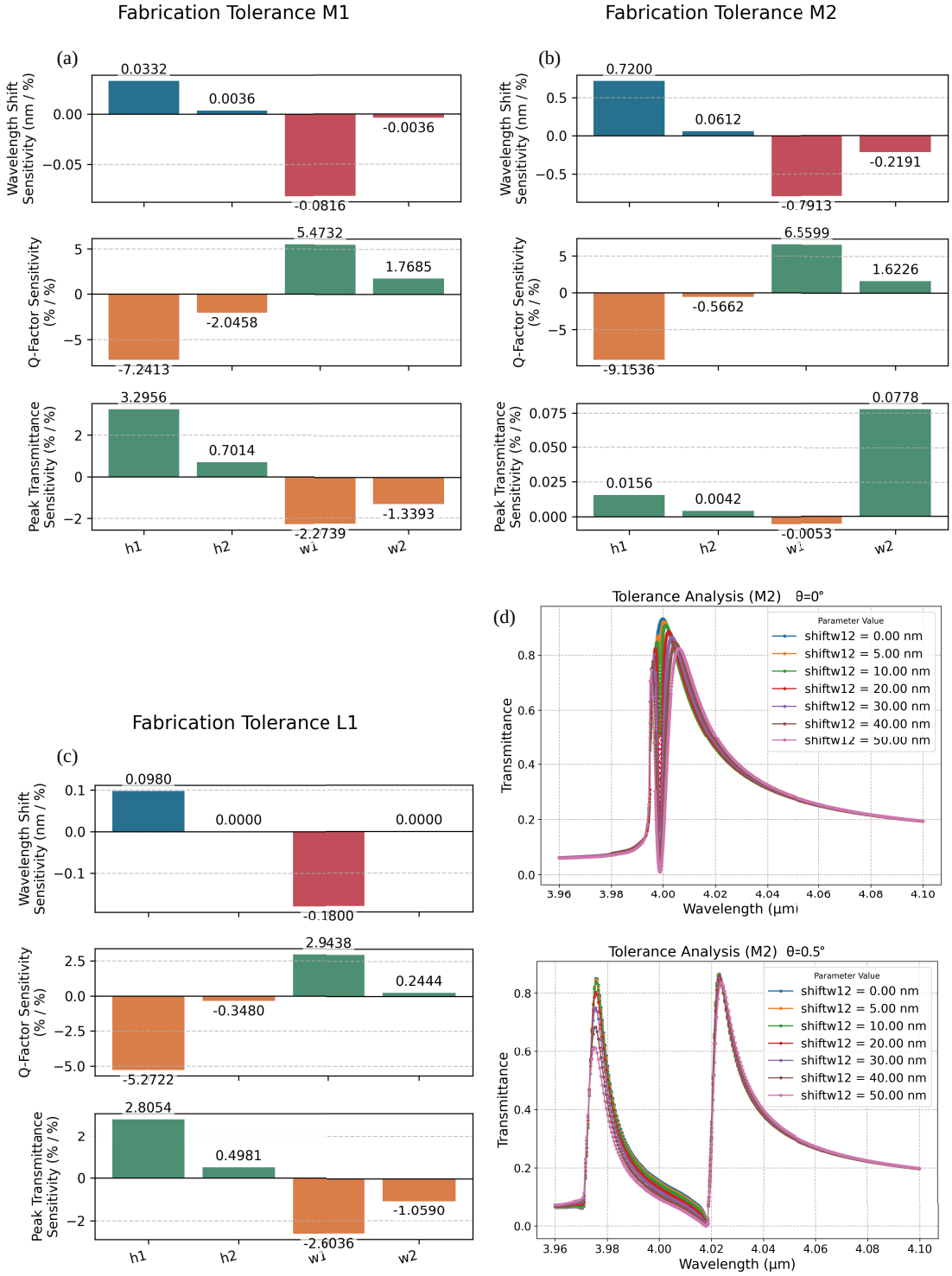

FIGURE 6. Summary of fabrication-tolerance analysis for the optimized dual-grating designs: (a) M_1, (b) M_2, and (c) L_1. Each chart shows the sensitivity of resonant wavelength (top), Q-factor (middle), and peak transmittance (bottom) to a 1% variation in key geometric parameters: slit widths, grating thicknesses, and corner radii (in the Supplementary). (d) Robustness of M_2 to lateral misalignment between the front and back gratings (Δx up to 50 nm), evaluated at normal incidence ($\theta = 0°$, upper plot) and at a slightly oblique incidence ($\theta = 0.5°$, lower plot).

We subjected the M_1 design to an exaggerated "stress test," independently sweeping the corner radii (r) for three distinct sites: the light-entry corners (r_3, front-air), the cavity internal corners (r_2, front-spacer), and the distal substrate interface (r_1, back-substrate). The quantitative results reveal that the device is remarkably robust against massive deformations of the input and cavity corners (r_3 and r_2); even with 100 nm rounding, the transmission remains high ($> 67\%$) and the resonant mode remains strongly excited. In stark contrast, the performance is exquisitely sensitive to the distal back-grating corner (r_1).

Rounding this interface causes a severe penalty in peak transmission ($\Delta T \approx 40\%$) and a suppression of the internal field. This confirms that the sharp discontinuity at the substrate-metal interface (r_1) is a primary active element mediating the critical matching, driving the resonance even when the device is illuminated from the front. Importantly, small corner radii corresponding to realistic fabrication imperfections ($r < 20\,\text{nm}$) do not substantially affect performance, ensuring high yield. Moreover, this hierarchy provides a clear fabrication strategy: process control should be focused on the first, simpler lithography step that defines the back grating (r_1), while the relaxed tolerance of the second layer de-risks the overall alignment and patterning process.

We further quantify robustness to possibly what one may consider the most challenging aspect of the fabrication process, the lithography overlay alignment errors by laterally shifting the front grating relative to the back by $\Delta x \in [0, 50]$ nm (steps of 5 and 10 nm). Fig. 6(d) highlights the impact of lateral misalignment on M_2 for two incidence conditions. At normal incidence ($\theta = 0°$), even small shifts between the gratings introduce a strong coupling asymmetry, which appears as an ultra-narrow dip in the transmission spectrum, effectively splitting the original peak into two closely spaced resonances. This behavior is attributed to enhanced absorption caused by imperfect mode matching when the gratings are misaligned. In contrast, at oblique incidence, the primary regime for angular sensing applications, the optical symmetry is already broken by the incident wavevector ($k_x \neq 0$) and the angular splitting inherent to the design dominates the response. Here, misalignment primarily reduces the amplitude of the shorter-wavelength branch, while the longer-wavelength branch remains almost unaffected. Overall, for the M_2, the degradation remains modest: T_{peak} decreases by less than 10% and Q by less than 15%, confirming that the dual-grating architecture maintains high performance under realistic overlay errors for both normal and oblique illumination. For the M_1 design at oblique incidence, the lateral misalignment even enhances the longer wavelength branch while damping shorter branch without altering the fundamental, high-Q EOT performance or the angular sensitivity. At normal incidence, the M_1 design exhibits a distinct peak splitting (Supplementary Fig. S15). While this could be considered a deterioration of the single-mode performance, the misalignment demands to avoid this are well within the "safe zone" of established nanofabrication protocols (discussed below).

Furthermore, we identify that this structural sensitivity at normal incidence can be strategically exploited. By introducing a *prescribed* lateral offset (symmetry breaking) between the gratings and reducing the front aperture ratio to 5%, the secondary spectral branch at oblique incidence can be suppressed. We propose a an optimized asymmetric MWIR configuration with period $\Lambda = 2.843\,\mu\text{m}$, grating thicknesses $h_1 = 125\,\text{nm}$ and $h_2 = 44\,\text{nm}$. A lateral offset of 10% ($\sim 284\,\text{nm}$) was introduced to break symmetry and suppress the secondary resonance branch. The transmission spectrum was calculated at an incidence angle of $\theta = 1.5°$. As detailed in Supplementary Fig. S17, this configuration achieves a solitary resonant peak (suppression of the secondary branch) with an improved average background floor ($< 2.5\%$) and dip ($< 0.5\%$). This corresponds to an average out-of-band rejection ratio (OBRR) floor of $> 14\,\text{dB}$ and peak-to-valley rejection ratio (PVRR) of $> 22\,\text{dB}$. The $> 60\%$ transmission resonance, shows a linewidth of FWHM $\approx 0.24\,\text{nm}$ ($Q > 17,000$). This confirms that intentional asymmetry is a viable route to achieving robust, high-contrast filtering suitable for isotope spectroscopy.

Finally, when comparing the overall robustness of the three structures, the M_2 design emerges as the most promising candidate if high transmission is the focal requirement. It exhibits the lowest transmission magnitude sensitivity to variations in all critical parameters. The other two designs offer very good robustness of their transmission peak wavelength, with very low wavelength sensitivity to all critical parameters. These properties align well with the design considerations of high-Q vs. high transmission of the three designs. This detailed analysis of fabrication tolerance is crucial to bridge the gap between theoretical design and practical implementation, a step often overlooked but essential for realization.

The proposed dual-grating architecture relies on established nanofabrication protocols involving sequential lithography and thin-film deposition, a methodology widely validated for complex multi-layer metasurfaces [55, 56]. To satisfy the refractive index matching required for the high-Q resonance, the metallic slits in both the bottom and top gratings must be filled with the dielectric material. This is achieved through a planarized backfill process, analogous to the Damascene techniques used in microelectronics. For the first layer, the back metal grating is patterned on the substrate (CaF_2/BaF_2) using lift-off. High-contrast fiducial alignment markers are fabricated on the wafer periphery during this step. The metallic voids are then backfilled with the dielectric spacer material. For polymeric spacers (e.g., PDMS), spin-coating naturally fills the trenches and planarizes the surface. For solid dielectrics, deposition is followed by Chemical Mechanical Polishing (CMP) or a flowable planarization step to expose the metal surface and establish a flat foundation for the subsequent layer [56]. Following the alignment and patterning of the top grating, a second deposition step fills the narrow top slits. To avoid a thick overcladding layer, a controlled etch-back process (e.g., Reactive Ion Etching) is employed to remove excess dielectric from the top surface, halting at the metal interface. Finally, a nanometric passivation layer (e.g., $< 5\,\text{nm}$ Al_2O_3 via ALD) can be applied to prevent silver tarnishing without optically affecting the resonant mode.

From a manufacturing perspective, the design is highly compatible with mass production. The smallest critical dimension (CD) in our optimized asymmetric design corresponds to the narrow front-grating slit. For the MWIR design ($\Lambda \approx 2.8\,\mu\text{m}$ with 5% aperture), the CD is approximately 140 nm. This dimension is well within the resolution limits of modern Deep-UV (DUV, 193 nm) photolithography, which routinely achieves overlay accuracies better than 5 nm [57], far superior to the $\sim$20 nm tolerance required for our device. Alternatively, for cost-effective large-area sensor fabrication, Nanoimprint Lithography (NIL) presents a compelling route, demonstrating both the required resolution and overlay alignment capabilities to replicate such dual-layer nanostructures at high throughput [58–61].

TABLE 2. Mid-IR plasmonic designs with high Q-factors (2015–2025), including experimental demonstrations and theoretical proposals. Mode: EOT — Transmission, Refl. = Reflection, Abso./Emis. = Absorption/Emission. Type: Exp. = Experimental, Th. = Theoretical.

Reference (Year)	Platform/Mechanism	Q	λ	Mode	Type
This Work (L_1)	Dual-grating plasmonic EOT	> 2000	10 μm	**EOT**	Sim./Th.
This Work (M_2)	Dual-grating plasmonic EOT	> 1000	4 μm	**EOT**	Sim./Th.
This Work (Asym. M_2) Fig. S17	Dual-grating (Symmetry-broken)	$> 17,000$	∼4 μm	**EOT**	Sim./Th.
Xu et al., JMCC (2025) [62]	3D Au MIM metasurface (quasi-BIC)	∼125	4.9 μm	Refl.	Exp.
Liu et al., APL (2020) [63]	MIM metasurface (hybridized dipoles)	60.2	3.63 μm	Refl.	Exp.
Xing et al., Plasmonics (2024) [64]	Split-ring metasurface (anapole)	35 (exp.), 88 (th.)	7.9 μm	Refl.	Exp./Th.
Ou et al., AIP Adv. (2022) [11]	Tamm plasmon absorber	144	2.73 μm	Abso.	Exp.
Xi et al., Opt. Lett. (2021) [12]	Tamm plasmon emitter	508	4.225 μm	Emis.	Th.
Dayal et al., JAP (2017) [65]	MIM cavity absorber	High-Q	mid-IR	Abso.	Exp.
Biswas et al., Nanophotonics (2024) [13]	Plasmonic quasi-BIC metasurface	∼938	mid-IR	Refl.	Th.
Liang et al., PRL (2024) [14]	Nonlocal plasmonic metasurface	> 1000 s	generalized	Refl.	Th.

3. DISCUSSION

To place our achievements in the context of the current state-of-the-art, we provide a quantitative comparison in Table 2. This table benchmarks our OGDs against the highest-performing high-Q-factor plasmonic designs reported in the literature over the recent years. For an exhaustive survey of recent *all-dielectric platforms*, please refer to the comprehensive tables provided by [21, 24].

The designs summarized in Table 2 highlight a critical distinction: nearly all high-Q plasmonic metasurfaces reported in the mid-IR operate in *reflection* or *absorption/emission* modes, such as Tamm plasmon absorbers and emitters or quasi-BIC metasurfaces. These platforms achieve narrow linewidths but do not provide high transmission through an opaque metal film. In contrast, our dual-grating architecture uniquely delivers ultra-high-Q resonances in *EOT* mode with near-unity throughput. This capability addresses a long-standing challenge in mid-IR plasmonics: combining high spectral selectivity (large Q) with efficient transmission, and full side-peak inhibition, which are all kept stable for remarkably wide θ and λ ranges. These are essential for integrated filtering, sensing, and free-space optical systems.

Furthermore, the Q factors of more than 2 k achieved by our L_1 design and over 16 k of the asymmetrical design are not only, to the best of our knowledge, among the highest Q-factors reported for MWIR/LWIR EOT through metal films, but also comparable with the record breaking Q factors of Mid-IR plamonics in absorption and reflection platforms. In this regard our work successfully translates the high-performance characteristics to the technologically vital but physically challenging MWIR and LWIR bands. The triple-coupling mechanism, enabled by the dual-grating architecture, provides a new and robust design paradigm to overcome the material limitations that have historically hindered plasmonic device performance at these longer wavelengths.

An all-dielectric counterpart would require a substantially thicker and more complex architecture to first establish the broadband mirror before a resonant transmission feature could be engineered. While hybridizing our dual-grating topology with dielectric resonators could theoretically enhance Q further, our plasmonic metamaterial presents a more compact and architecturally efficient solution for creating high-performance EOT-based filters. This highlights the fundamental elegance and efficiency of our plasmonic approach, yielding the desired broadband rejection and narrow-band transmission within a total thickness of a few hundred nanometers.

The unique optical characteristics of the investigated OGDs enable their integration into diverse functional setups, as illustrated in Figs. 7–8. For instance, under monochromatic illumination with finite angular divergence ($\Delta\theta_{\text{in}}$), the structure facilitates high-precision angular sensing or collimation filtering (Fig. 7). Alternatively, for broadband radiation, the device functions as a highly tunable spectral filter, where the resonant wavelength λ_0 is dynamically selected by altering the angle of incidence θ_{in} (or tilting the device). Furthermore, the strong angular dispersion allows the design to operate as a prism-like spatial-spectral beam comb, transmitting separate beams with corresponding pairs of directions and wavelengths (θ_i, λ_i), see Fig. 8.

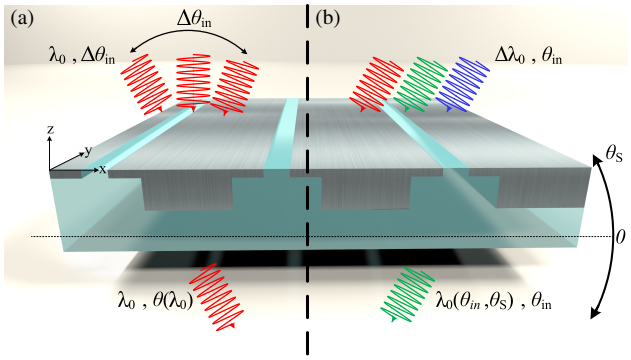

FIGURE 7. Two representative OGD-based configurations for spectra-angular functionality: (a) monochromatic illumination with a finite angular spread, enabling angular discrimination or collimation filtering; (b) polychromatic illumination at a fixed incidence angle θ_{in} for narrowband spectral selection.

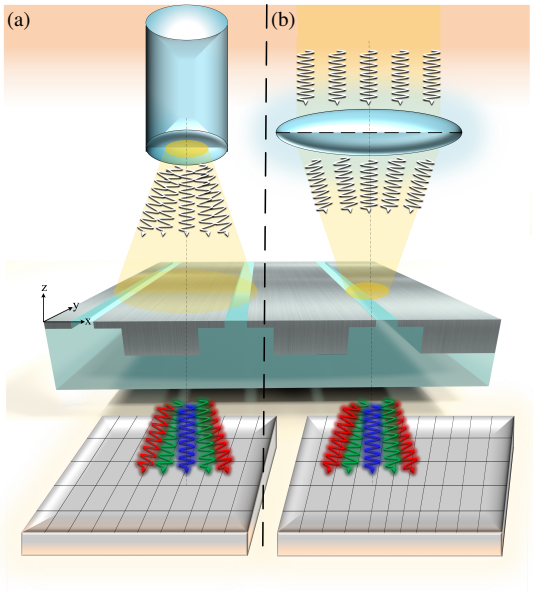

FIGURE 8. Proposed OGD-integrated instrumentation for polychromatic, multi-angular spectral-angular sensing: (a) configuration using a diverging beam emitted from an optical fiber; (b) configuration after beam conditioning with focusing optics for controlled angular distribution.

A primary motivation of this research was to translate the rich sensing capabilities of plasmonic EOT, well-established in the visible and near-infrared, deep into the mid- and far-infrared regimes. Consequently, the specific use-cases highlighted below represent only a subset of the potential utility. We anticipate that with appropriate optical instrumentation, this platform will unlock further novel sensing and control modalities. Here, by manipulating the upgraded trade-off between T and Q, and exploiting the symmetry-dependent mode splitting, we detail a few distinct exemplary applications.

Precision Direction-of-Arrival (DoA) Sensing: The strong angular dispersion, robust over a significant λ-θ range (see Supplementary Fig. S16 and Table S1), of the OGD highly benefit application in angular sensing and Laser Warning Receivers (LWR). Unlike dielectric interference filters where the wavelength shift scales quadratically with angle ($\Delta\lambda \propto \theta^2/n^2$), resulting in negligible sensitivity at normal incidence ($S \approx 0$), the OGD follows the linear Wood's anomaly condition: $\lambda^{\pm} \approx \Lambda(n_{\text{eff}} \pm \sin\theta)$. The angular sensitivity (S) at normal incidence can be explicitly calculated as the derivative of the resonant wavelength with respect to the incidence angle. For the L_1 design for example, ($\Lambda = 7.692\,\mu\text{m}$), operating in air ($n = 1$):

$$S = \left|\frac{d\lambda}{d\theta}\right|_{\theta=0} \approx \Lambda\cos(0)\cdot\frac{\pi}{180^\circ}$$

$$\approx 7692\,\text{nm} \times 0.01745\,\text{rad}/^\circ \approx 134\,\text{nm}/^\circ. \quad (6)$$

This linear sensitivity is over two orders of magnitude higher than that of standard interference filters. While standard imaging systems rely on bulky optics to map angle to position, recent works have demonstrated the concept of "Angle-Sensitive Pixels" (ASPs) using nanostructured arrays to encode angular information directly into the detector's response [66, 67]. Similarly, on-chip spectral reconstruction has been achieved using mosaic arrays of photonic crystals [68]. Building on these concepts, our symmetric dual-grating design offers a promising platform for mid-infrared DoA sensing. By utilizing a "super-pixel" architecture composed of spectrally detuned OGD elements, the system can decouple the spectral content from incidence angle without refractive optics. Crucially, our design leverages the intrinsic symmetry of the structure: oblique incidence splits the resonance into two branches (λ^+ and λ^-). Tracking $\Delta\lambda$ (see Eq. (4) and Figs. S16–S17) between these branches provides a differential measurement with doubled sensitivity ($S_{diff} \approx 268\,\text{nm}/^\circ$) that encodes the angle of arrival. Simultaneously, the unknown source wavelength is retrieved via the spectral centroid ($\lambda_c \approx (\lambda^+ + \lambda^-)/2$). By independently monitoring both the separation (angle) and the average spectral position (wavelength) across the graded array, the system can resolve the two unknown variables of the source. This differential scheme is inherently self-referencing; since environmental temperature fluctuations induce a common-mode spectral shift in both branches due to the thermo-optic effect, measuring the difference $\Delta\lambda$ effectively cancels out thermal drift. This enables robust, high-precision angular tracking LWR and situational awareness systems with a small form factor, overcoming the thermal instability limitations of conventional narrowband filters.

Furthermore, the differential measurement scheme inherently mitigates the limitation of the Fano resonance lineshape (i.e., the non-zero background continuum). Since the background leakage is spectrally broadband and affects both resonant branches symmetrically, it acts as a common-mode signal. By tracking $\Delta\lambda$ or the differential intensity ratio rather than absolute radiometric power, the system effectively filters out this broadband background. This converts the sensing mechanism from an intensity-based measurement, susceptible to background noise, to a spectral-position measurement, thereby achieving high Signal-to-Noise Ratio (SNR), even in the presence of the characteristic Fano continuum [69].

Spatio-Spectral Imaging via Angular Dispersion: A complementary application leverages this same physical mechanism to solve the inverse problem: determining the spectral composition of a scene using defined optics. This is particularly relevant for the "broadband" M_2 design in the MWIR (3–5 µm). While standard imaging strives for spectral uniformity, here we exploit the strong angular dispersion to enable *Spatio-Spectral Encoding*. By coupling the sensor array with a standard wide-angle lens, e.g., Fig. 8, which maps incidence angles to spatial pixel positions, the resonant wavelength is deterministically coupled to the field angle. As demonstrated in the broadband spectral analysis (Fig. 2 and Supplementary Fig. S16(a)), the resonant splitting into upper (λ^+) and lower (λ^-) branches effectively "sweeps" across the entire MWIR band (3–5 µm) over an angular range of $\pm 10^\circ$ if oriented off-axis, allowing different pixels to sample different spectral bands simultaneously. Crucially, the dual-peak resonance inherent to the symmetric design plays a vital role in noise rejection by creating a unique spatial signature. Since the filter exhibits two transmission branches (λ^+ and λ^-), a

monochromatic target signal (e.g., a gas emission line) will be registered at two distinct radial positions on the sensor array, corresponding to the specific angles where each branch matches the target wavelength. This creates a built-in validation mechanism: true spectral signals must appear as correlated pairs (e.g., concentric rings), whereas broadband thermal background (clutter) affects all pixels continuously. Furthermore, since the thermal background varies slowly across the angular domain, adjacent pixels, which sample wavelengths slightly detuned from the target line, serve as intrinsic reference channels. By subtracting this common-mode baseline measured by neighboring elements, the mechanism inherently filters out the broadband noise floor, enhancing the Signal-to-Clutter Ratio (SCR) for identifying specific material signatures within a complex thermal scene.

Compact Isotope-Resolved Gas Sensing: While broad spectral features characterize solids and liquids, gas-phase sensing often requires resolving fine rotational-vibrational structures. A particularly challenging frontier is isotope-resolved sensing. These isotopic signatures are separated by small spectral shifts (typically $< 1\,\text{nm}$), rendering them indistinguishable to standard sensors equipped with broad interference filters. For example, distinguishing the P-branch rotational lines of $^{13}CO_2$ (centered near $4.38\,\mu\text{m}$) from the dominant $^{12}CO_2$ background,for medical breath diagnostics or environmental tracing, requires resolving spectral shifts often smaller than 1–2 nm. Our symmetry-broken mode can potentially disrupt this paradigm. By achieving a single-mode resonance with a theoretical scientific-grade Q-factor of $> 16,000$ (FWHM $\approx 0.24\,\text{nm}$), as demonstrated in Supplementary Fig. S17, the device offers sufficient resolution to isolate specific isotopic absorption lines. The engineered asymmetry suppresses the secondary spectral branch, preventing the spectral-crosstalk from the abundant isotope. Combined with the high PVRR ($> 22\,\text{dB}$), this architecture potentially enables the realization of miniaturized, low-cost sensors capable of quantitative isotope ratio analysis, a capability previously restricted to bench-top spectrometers.

Secure, Noise-Resilient Free-Space Optics (FSO): For Mid-IR optical communication links, the OGD offers a dual advantage of high throughput and spatial-spectral filtering. First, the $> 80\%$ transmission efficiency minimizes insertion loss, which is critical for long-range links limited by atmospheric attenuation. Second, the device's strong angular dispersion can be exploited to enhance SNR. Unlike standard interference filters that accept all incident light within the spectral passband regardless of angle, the OGD imposes a strict angular-spectral condition: light is transmitted only if it satisfies the specific (λ, θ) coupling resonance (see Figs. 7–8). Consequently, while the collimated laser signal (aligned to the resonance angle) is transmitted efficiently, broadband background radiation (e.g., solar or thermal clutter) incident from off-axis angles is rejected — even if it spectrally overlaps with the laser wavelength. This effectively acts as a passive spatial filter, improving the link margin. Furthermore, the symmetric mode's spectral splitting sensitivity ($\Delta\lambda \propto \theta$) can serve as an integrated alignment error sensor, allowing the receiver to detect micron-scale beam wander or vibrations by monitoring the spectral line shape, thereby facilitating active beam stabilization.

Material Versatility and Lab-on-Chip Integration: Finally, we highlight a structural advantage relevant to biochemical sensing. The refractive index of the substrates employed in this work ($n \approx 1.3$–1.45) closely matches that of common optical polymers (e.g., PDMS, PMMA) and various biological fluids. Since the high-Q resonance is tightly confined within the dielectric spacer layer, this index compatibility suggests that the solid spacer could be substituted with a matched microfluidic channel without disrupting the optical impedance matching. This opens a pathway for transforming the dual-grating architecture into a flow-through refractive index sensor, enabling real-time, label-free monitoring of analytes in a Lab-on-Chip platform compatible with standard soft-lithography processes.

While the presented dual-grating designs achieve competitive rejection ratios with a compact architecture, specific high-performance applications may require greater optical density (OD). The proposed platform is potentially scalable to cascaded architectures, where two OGD units are stacked in series (separated by a dielectric buffer). Due to the multiplicative nature of optical transmission, a double-stack configuration would theoretically double the rejection ratio while maintaining a high peak transmission ($\sim 0.9^2 \approx 81\%$). This scalability is particularly relevant for cooled radiometric imaging and Mid-IR FSO communications, where steep spectral roll-offs and background suppression are prerequisites for minimizing channel crosstalk and detector saturation.

A fundamental characteristic of the proposed 1D dual-grating architecture is its dependence on polarization. Consequently, the device functions as an integrated linear polarizer, limiting the theoretical maximum system efficiency to 50% for unpolarized thermal sources, see s-polarization reflection spectra in Fig. S19. While this flux reduction is a trade-off, it enables the capability for *polarimetric thermography*, enhancing the contrast of man-made targets against natural backgrounds. For applications where polarization independence is paramount, the proposed topology can theoretically be generalized to a 2D cross-grating structure (e.g., a fishnet or hole array). However, the design and rigorous optimization of such geometries require fully three-dimensional full-wave simulations, which for Mid-IR plasmonic designs, entail a computational complexity orders of magnitude higher than the 2D invariant models employed here. Consequently, the translation of the "triple-coupling" mechanism to polarization-independent 3D architectures remains a challenging and exciting avenue for future development.

In conclusion, a broadly applicable concept for designing high-performance mid-infrared plasmonic devices is introduced. The dual-grating architecture, guided by the principle of decoupled mode engineering, provides an integrated solution to the challenges of EOT, delivering unprecedented Q-factors and transmission efficiencies. The designs are based on simple geometries and conventional materials, making them compatible with established nanofabrication techniques and paving the way for a new generation of ultra-compact, high-performance infrared photonic components, effectively

translating the versatility of visible-range plasmonic EOT to the thermal infrared regime.

4. METHODS

The eigenvalue problems for EM BEMs in the grating regions due to [70–72] and the search for the eigenvalue confluences were solved with built-in `fzero` and `fsolve` MATLAB codes.

The far-field response, EM fields, and power density simulations, as well as computer-aided design, were done with an in-house improved version of the rigorous coupled wave analysis (RCWA) code. This code is enhanced for modeling metallic structures, which are notoriously challenging for standard RCWA implementations. This includes: (i) an in-layer S-matrix propagation algorithm [73], which furnishes unconditional numerical stability; (ii) Fourier-factorization rules recast to achieve convergence with increasing truncation order, due to line and zigzag inverse Laurent rules [73–77] and [77, 78], respectively, and to the normal-vector method [79–81]. These codes are integrated with trial-and-error automated multi-start optimization routines [82, 83] implemented in the MATLAB Optimization Toolbox [84], while our GUI drives the entire software package, managing the input/output. This integrated approach enables performing the computer-aided design of the multi-layered grating structures with a predefined optimal far-field response. Although RCWA has frequently been reported to display very slow convergence for structures merging metal gratings with TM-polarized irradiation, a symbiosis of an improved version and tailored implementation of MATLAB codes made our computer-aided design process highly efficient. To demonstrate the stability of the high-Q results, we performed a convergence test varying the truncation order (N) of the Fourier harmonics shown in the Supplementary Fig. S22. For the final results presented in the manuscript, we utilized a high truncation order of $N = 300$ (corresponding to $2N+1 = 601$ Fourier harmonics) for spectral scans, which also agreed well with FEM simulations, ensuring high fidelity, and up to $N = 700$ for field profiles.

We cross-validate RCWA and FEM results for each nominal design. FEM simulations (COMSOL 6.1) utilized a physics-controlled "Extremely Fine" mesh, with manual refinement at the sharp metallic corners (maximum element size < 1 nm) to accurately resolve field singularities. The simulation domain included a thick substrate ($\sim 30\lambda_0$) to capture the full decay of the SPP modes, terminated vertically by periodic ports and laterally by Floquet periodic conditions to rigorously account for all diffracted orders propagating to infinity. Energy conservation was enforced until $\max_{\lambda,\theta} |R+T+A-1| < 10^{-4}$ over the simulated grids, with typical residuals $\ll 10^{-6}$. Fig. S9 overlays the RCWA and FEM spectra at normal incidence for designs $M_1/M_2/L_1$, showing excellent agreement in both peak position and lineshape (RMSEs: $M_1 < 2 \times 10^{-2}$, $M_2 < 1.2 \times 10^{-2}$, $L_1 < 4.2 \times 10^{-2}$).

To investigate fabrication tolerance, a series of parametric sweeps were performed for each critical geometric dimension ($\pm 5\%$ deviation for thicknesses and widths; absolute values of 10, 20, and 30 nm for corner radii). The resulting spectral data was exported and analyzed using a custom Python script. Key performance metrics, including the resonant wavelength (λ_{res}), peak transmittance (T_p), and quality factor (Q-factor), were extracted for each simulation. The sensitivity of each metric to a given geometric parameter was then quantified. For each parameter scan, a first-order polynomial was fitted to the data points of the calculated metric versus the percentage change in the parameter. The slope of this line was taken as the sensitivity factor, representing the average change in the metric for a 1% change in the parameter (e.g., in units of nm/% for wavelength shift or %/% for normalized metric like Q-factor).

REFERENCES

[1] Stanley, R., "Plasmonics in the mid-infrared," *Nature Photonics*, Vol. 6, No. 7, 409–411, 2012.

[2] Brolo, A. G., "Plasmonics for future biosensors," *Nature Photonics*, Vol. 6, No. 11, 709–713, 2012.

[3] Li, S., Y. Fang, and J. Wang, "Control of light-matter interactions in two-dimensional materials with nanoparticle-on-mirror structures," *Opto-Electronic Science*, Vol. 3, No. 7, 240011, 2024.

[4] Chen, Y., F. Zhang, Z. Dang, X. He, C. Luo, Z. Liu, P. Peng, Y. Dai, Y. Huang, Y. Li, and Z. Fang, "Chiral detection of biomolecules based on reinforcement learning," *Opto-Electronic Science*, Vol. 2, No. 1, 220 019–1–220 019–10, 2023.

[5] Lochbihler, H. and R. Depine, "Highly conducting wire gratings in the resonance region," *Applied Optics*, Vol. 32, No. 19, 3459–3465, 1993.

[6] Ebbesen, T. W., H. J. Lezec, H. F. Ghaemi, T. Thio, and P. A. Wolff, "Extraordinary optical transmission through sub-wavelength hole arrays," *Nature*, Vol. 391, No. 6668, 667–669, 1998.

[7] Ghaemi, H. F., T. Thio, D. E. Grupp, T. W. Ebbesen, and H. J. Lezec, "Surface plasmons enhance optical transmission through subwavelength holes," *Physical Review B*, Vol. 58, No. 11, 6779–6782, Sep. 1998.

[8] Grupp, D. E., H. J. Lezec, T. Thio, and T. W. Ebbesen, "Beyond the Bethe limit: Tunable enhanced light transmission through a single sub-wavelength aperture," *Advanced Materials*, Vol. 11, No. 10, 860–862, 1999.

[9] Qi, X., L. A. Pérez, M. I. Alonso, and A. Mihi, "High Q-factor plasmonic surface lattice resonances in colloidal nanoparticle arrays," *ACS Applied Materials & Interfaces*, Vol. 16, No. 1, 1259–1267, 2024.

[10] Bin-Alam, M. S., O. Reshef, Y. Mamchur, M. Z. Alam, G. Carlow, J. Upham, B. T. Sullivan, J.-M. Ménard, M. J. Huttunen, R. W. Boyd, and K. Dolgaleva, "Ultra-high-Q resonances in plasmonic metasurfaces," *Nature Communications*, Vol. 12, No. 1, 974, Feb. 2021.

[11] Ou, C., J. Wang, C. Sun, Z. Hao, Y. Han, B. Xiong, L. Wang, H. Li, J. Yu, and Y. Luo, "A high-Q mid-infrared Tamm plasmon absorber using MgF_2 and Ge aperiodic tandem films designed by the genetic algorithm," *AIP Advances*, Vol. 12, No. 3, 035052, 2022.

[12] Xi, W., Y. Liu, J. Song, R. Hu, and X. Luo, "High-throughput screening of a high-Q mid-infrared Tamm emitter by material informatics," *Optics Letters*, Vol. 46, No. 4, 888–891, 2021.

[13] Biswas, S. K., W. Adi, A. Beisenova, S. Rosas, E. R. Arvelo, and F. Yesilkoy, "From weak to strong coupling: Quasi-BIC metasurfaces for mid-infrared light-matter interactions," *Nanophotonics*, Vol. 13, No. 16, 2937–2949, 2024.

[14] Liang, Y., D. P. Tsai, and Y. Kivshar, "From local to nonlocal high-Q plasmonic metasurfaces," *Physical Review Letters*, Vol.

133, No. 5, 053801, Jul. 2024.
[15] Park, J., J.-H. Kang, X. Liu, S. J. Maddox, K. Tang, P. C. McIntyre, S. R. Bank, and M. L. Brongersma, "Dynamic thermal emission control with InAs-based plasmonic metasurfaces," *Science Advances*, Vol. 4, No. 12, eaat3163, 2018.
[16] Kim, S., M. S. Jang, V. W. Brar, K. W. Mauser, L. Kim, and H. A. Atwater, "Electronically tunable perfect absorption in graphene," *Nano Letters*, Vol. 18, No. 2, 971–979, 2018.
[17] Law, S., D. C. Adams, A. M. Taylor, and D. Wasserman, "Mid-infrared designer metals," *Optics Express*, Vol. 20, No. 11, 12 155–12 165, 2012.
[18] Zhong, Y., S. D. Malagari, T. Hamilton, and D. M. Wasserman, "Review of mid-infrared plasmonic materials," *Journal of Nanophotonics*, Vol. 9, No. 1, 093791, 2015.
[19] Luo, X., "Principles of electromagnetic waves in metasurfaces," *Science China Physics, Mechanics & Astronomy*, Vol. 58, No. 9, 594201, Sep. 2015.
[20] Guo, Y., X. Ma, M. Pu, X. Li, Z. Zhao, and X. Luo, "High-efficiency and wide-angle beam steering based on catenary optical fields in ultrathin metalens," *Advanced Optical Materials*, Vol. 6, No. 19, 1800592, 2018.
[21] Fang, J., R. Chen, D. Sharp, E. M. Renzi, A. Manna, A. Kala, S. A. Mann, K. Yao, C. Munley, H. Rarick, *et al.*, "Million-Q free space meta-optical resonator at near-visible wavelengths," *Nature Communications*, Vol. 15, No. 1, 10341, Nov. 2024.
[22] Hsu, C. W., B. Zhen, A. D. Stone, J. D. Joannopoulos, and M. Soljačić, "Bound states in the continuum," *Nature Reviews Materials*, Vol. 1, No. 9, 16048, Jul. 2016.
[23] Avrahamy, R., B. Milgrom, M. Zohar, and M. Auslender, "Chalcogenide-based, all-dielectric, ultrathin metamaterials with perfect, incidence-angle sensitive, mid-infrared absorption: Inverse design, analysis, and applications," *Nanoscale*, Vol. 13, 11 455–11 469, 2021.
[24] Watanabe, K., T. Nagao, and M. Iwanaga, "Low-contrast BIC metasurfaces with quality factors exceeding 100,000," *Nano Letters*, Vol. 25, No. 7, 2777–2784, 2025.
[25] Porto, J. A., F. J. García-Vidal, and J. B. Pendry, "Transmission resonances on metallic gratings with very narrow slits," *Physical Review Letters*, Vol. 83, No. 14, 2845–2848, Oct. 1999.
[26] De Abajo, F. J. G., "Colloquium: Light scattering by particle and hole arrays," *Reviews of Modern Physics*, Vol. 79, No. 4, 1267–1290, Oct. 2007.
[27] Lalanne, P., J. P. Hugonin, H. T. Liu, and B. Wang, "A microscopic view of the electromagnetic properties of sub-λ metallic surfaces," *Surface Science Reports*, Vol. 64, No. 10, 453–469, 2009.
[28] Garcia-Vidal, F. J., L. Martin-Moreno, T. W. Ebbesen, and L. Kuipers, "Light passing through subwavelength apertures," *Reviews of Modern Physics*, Vol. 82, No. 1, 729–787, Mar. 2010.
[29] Law, S., V. Podolskiy, and D. Wasserman, "Towards nano-scale photonics with micro-scale photons: The opportunities and challenges of mid-infrared plasmonics," *Nanophotonics*, Vol. 2, No. 2, 103–130, 2013.
[30] Rodrigo, S. G., F. d. León-Pérez, and L. Martín-Moreno, "Extraordinary optical transmission: Fundamentals and applications," *Proceedings of the IEEE*, Vol. 104, No. 12, 2288–2306, Dec. 2016.
[31] Liu, H. and P. Lalanne, "Microscopic theory of the extraordinary optical transmission," *Nature*, Vol. 452, No. 7188, 728–731, 2008.
[32] Liu, H. and P. Lalanne, "Comprehensive microscopic model of the extraordinary optical transmission," *Journal of the Optical Society of America A*, Vol. 27, No. 12, 2542–2550, 2010.
[33] Cao, Q. and P. Lalanne, "Negative role of surface plasmons in the transmission of metallic gratings with very narrow slits," *Physical Review Letters*, Vol. 88, No. 5, 057403, Jan. 2002.
[34] Lochbihler, H. and R. A. Depine, "Properties of TM resonances on metallic slit gratings," *Applied Optics*, Vol. 51, No. 11, 1729–1741, 2012.
[35] Babar, S. and J. H. Weaver, "Optical constants of Cu, Ag, and Au revisited," *Applied Optics*, Vol. 54, No. 3, 477–481, 2015.
[36] Franta, D., D. Nečas, A. Giglia, P. Franta, and I. Ohlídal, "Universal dispersion model for characterization of optical thin films over wide spectral range: Application to magnesium fluoride," *Applied Surface Science*, Vol. 421, 424–429, 2017.
[37] "Magnesium fluoride (MgF_2) optical material — Data sheet," https://www.crystran.com/optical-materials/magnesium-fluoride-mgf2, transmission 0.12–7 µm, Aug. 2025.
[38] Li, H. H., "Refractive index of alkaline earth halides and its wavelength and temperature derivatives," *Journal of Physical and Chemical Reference Data*, Vol. 9, No. 1, 161–290, 1980.
[39] "Teflon™ AF amorphous fluoroplastic resins: Product information," https://www.teflon.com/en/-/media/files/teflon/teflon-af-product-info.pdf, optical transmission from IR to UV; $n \approx 1.29$–1.31, Aug. 2025.
[40] "Teflon® AF overview (AF1600/AF2400)," https://www.professionalplastics.com/professionalplastics/content/downloads/TeflonAF16002400Data.pdf, processing/use temperature guidance; decomposition $> 360^{\circ}$C, Aug. 2025.
[41] "Calcium fluoride (CaF_2) optical material — Data sheet," https://www.crystran.com/optical-materials/calcium-fluoride-caf2, Aug. 2025.
[42] "Calcium fluoride windows — Transmission and specs," https://www.thorlabs.com/newgrouppage9.cfm?objectgroup_id=3978, Aug. 2025.
[43] Crystal GmbH, "Barium Fluoride (BaF_2) Optical Data," https://crystal-gmbh.com/shared/downloads/datenblaetter/optics_de/Bariumfluorid_Barium_Fluoride_BaF2.pdf, datasheet.
[44] ISP Optics, "Barium Fluoride (BaF_2) Transmission Curve Datasheet," https://www.lakeshore.com/docs/default-source/default-document-library/barium-fluoride-baf2-transmission-curve-datasheet.pdf, hosted by Lake Shore Cryotronics.
[45] "Barium fluoride (BaF_2) optical material — Data sheet," https://www.crystran.com/optical-materials/barium-fluoride-baf2, transmission 0.15–12 µm, Aug. 2025.
[46] "Cryolite patinal® (Na_3AlF_6) thin-film data sheet," https://www.merckgroup.com/Products/PM/global/106457_Na3AlF6_tcm20 33-en.pdf, transparency ∼200 nm–14 µm; thin-film $n \approx 1.32$–1.35, Aug. 2025.
[47] Lalanne, P., C. Sauvan, J. P. Hugonin, J. C. Rodier, and P. Chavel, "Perturbative approach for surface plasmon effects on flat interfaces periodically corrugated by subwavelength apertures," *Physical Review B*, Vol. 68, No. 12, 125404, Sep. 2003.
[48] Alù, A., "Restoring the physical meaning of metamaterial constitutive parameters," *Physical Review B*, Vol. 83, 081102, 2011.
[49] Alù, A., "First-principles homogenization theory for periodic metamaterials," *Physical Review B*, Vol. 84, No. 7, 075153, 2011.
[50] Caloz, C., A. Alù, S. Tretyakov, D. Sounas, K. Achouri, and Z.-L. Deck-Léger, "Electromagnetic nonreciprocity," *Physical Review Applied*, Vol. 10, No. 4, 047001, 2018.
[51] Miri, M.-A., F. Ruesink, E. Verhagen, and A. Alù, "Optical nonreciprocity based on optomechanical coupling," *Physical Review Applied*, Vol. 7, No. 6, 064014, 2017.
[52] Wang, X., A. Díaz-Rubio, H. Li, S. A. Tretyakov, and A. Alù, "Theory and design of multifunctional space-time metasur-

faces," *Physical Review Applied*, Vol. 13, No. 4, 044040, 2020.

[53] Strelniker, Y. M. and D. J. Bergman, "Itinerant versus localized plasmons in an assembly of metal-dielectric parallel flat slabs in the presence of a perpendicular magnetic field: Faraday and magneto-optical Kerr effects," *Physical Review B*, Vol. 103, No. 20, 205302, May 2021.

[54] Strelniker, Y. M. and D. J. Bergman, "Optical transmission through metal films with a subwavelength hole array in the presence of a magnetic field," *Physical Review B*, Vol. 59, No. 20, R12763, May 1999.

[55] Liu, N., H. Guo, L. Fu, S. Kaiser, H. Schweizer, and H. Giessen, "Three-dimensional photonic metamaterials at optical frequencies," *Nature Materials*, Vol. 7, No. 1, 31–37, 2008.

[56] Chang, Z., R. Huang, P. Chen, and G. Li, "Shaping light with multilayer metasurfaces: Design, fabrication, and applications," *Journal of Physics D: Applied Physics*, Vol. 58, No. 44, 443003, Oct. 2025.

[57] ASML, "ASML TWINSCAN NXT: 1980Di Immersion Scanner Datasheet," dedicated Chuck Overlay $\leq$ 2.5 nm, [Online]. Available: https://www.asml.com/en/products/duv-lithography-systems, 2024.

[58] Traub, M. C., W. Longsine, and V. N. Truskett, "Advances in nanoimprint lithography," *Annual Review of Chemical and Biomolecular Engineering*, Vol. 7, No. 1, 583–604, 2016.

[59] Einck, V. J., M. Torfeh, A. McClung, D. E. Jung, M. Mansouree, A. Arbabi, and J. J. Watkins, "Scalable nanoimprint lithography process for manufacturing visible metasurfaces composed of high aspect ratio TiO_2 meta-atoms," *ACS Photonics*, Vol. 8, No. 8, 2400–2409, 2021.

[60] Cox, L. M., A. M. Martinez, A. K. Blevins, N. Sowan, Y. Ding, and C. N. Bowman, "Nanoimprint lithography: Emergent materials and methods of actuation," *Nano Today*, Vol. 31, 100838, 2020.

[61] Shudo, S., H. Torii, Y. Suzaki, A. Kimura, K. Yamamoto, M. Hiura, K. Sakai, and Y. Takabayashi, "Nanoimprint performance improvements for high volume semiconductor device manufacturing," in *Photomask Japan 2024: XXX Symposium on Photomask and Next-Generation Lithography Mask Technology*, Vol. 13177, 42–49, Japan, 2024.

[62] Xu, H.-L., Z.-M. Meng, Y.-H. Liu, J.-Y. Su, Z.-Z. Fang, and J.-Y. Zhou, "Mid-infrared bifunctional high-Q plasmonic metasurfaces with strong intrinsic chirality and imaging-based biosensing," *Journal of Materials Chemistry C*, 2025.

[63] Liu, L., Z. Li, C. Cai, W. Zhu, X. Zheng, W. Zhang, J. Xu, and Z. Liu, "High-Q hybridized resonance in a plasmonic metasurface of asymmetric aligned magnetic dipoles," *Applied Physics Letters*, Vol. 117, No. 8, 081108, 2020.

[64] Xing, L., Q. Wulan, J. Yu, and Z. Liu, "Plasmonic anapole mode in a mid-infrared metasurface with improved quality factor," *Plasmonics*, Vol. 20, No. 6, 3733–3740, 2025.

[65] Dayal, G., A. Solanki, X. Y. Chin, T. C. Sum, C. Soci, and R. Singh, "High-Q plasmonic infrared absorber for sensing of molecular resonances in hybrid lead halide perovskites," *Journal of Applied Physics*, Vol. 122, No. 7, 073101, 2017.

[66] Yi, S., M. Zhou, Z. Yu, P. Fan, N. Behdad, D. Lin, K. X. Wang, S. Fan, and M. Brongersma, "Subwavelength angle-sensing photodetectors inspired by directional hearing in small animals," *Nature Nanotechnology*, Vol. 13, No. 12, 1143–1147, 2018.

[67] Avrahamy, R., M. Zohar, B. Milgrom, and M. Auslender, "Mid-infrared photodetector spectrometer concept based on ultrathin all-dielectric metamaterial with azimuth-incidence-angle tuned perfect optical absorption: Design and analysis," *Materials & Design*, Vol. 245, 113298, 2024.

[68] Wang, Z., S. Yi, A. Chen, M. Zhou, T. S. Luk, A. James, J. Nogan, W. Ross, G. Joe, A. Shahsafi, K. X. Wang, M. A. Kats, and Z. Yu, "Single-shot on-chip spectral sensors based on photonic crystal slabs," *Nature Communications*, Vol. 10, No. 1, 1020, Mar. 2019.

[69] Miroshnichenko, A. E., S. Flach, and Y. S. Kivshar, "Fano resonances in nanoscale structures," *Reviews of Modern Physics*, Vol. 82, No. 3, 2257–2298, Aug. 2010.

[70] Andrewartha, J. R., G. H. Derrick, and R. C. McPhedran, "A general modal theory for reflection gratings," *Optica Acta: International Journal of Optics*, Vol. 28, No. 11, 1501–1516, 1981.

[71] Sheng, P., R. S. Stepleman, and P. N. Sanda, "Exact eigenfunctions for square-wave gratings: Application to diffraction and surface-plasmon calculations," *Physical Review B*, Vol. 26, No. 6, 2907–2916, Sep. 1982.

[72] Li, L., "A modal analysis of lamellar diffraction gratings in conical mountings," *Journal of Modern Optics*, Vol. 40, No. 4, 553–573, 1993.

[73] Auslender, M. and S. Hava, "Scattering-matrix propagation algorithm in full-vectorial optics of multilayer grating structures," *Optics Letters*, Vol. 21, No. 21, 1765–1767, 1996.

[74] Lalanne, P. and G. M. Morris, "Highly improved convergence of the coupled-wave method for TM polarization," *Journal of the Optical Society of America A*, Vol. 13, No. 4, 779–784, 1996.

[75] Granet, G. and B. Guizal, "Efficient implementation of the coupled-wave method for metallic lamellar gratings in TM polarization," *Journal of the Optical Society of America A*, Vol. 13, No. 5, 1019–1023, 1996.

[76] Li, L., "Use of Fourier series in the analysis of discontinuous periodic structures," *Journal of the Optical Society of America A*, Vol. 13, No. 9, 1870–1876, 1996.

[77] Li, L., "Mathematical reflections on the fourier modal method in grating theory," in *Mathematical Modeling in Optical Science*, 111–139, G. Bao, L. Cowsar, and W. Masters (eds.), SIAM, Philadelphia, 2001.

[78] Li, L., "New formulation of the fourier modal method for crossed surface-relief gratings," *Journal of the Optical Society of America A*, Vol. 14, No. 10, 2758–2767, 1997.

[79] Popov, E. and M. Nevière, "Maxwell equations in Fourier space: Fast-converging formulation for diffraction by arbitrary shaped, periodic, anisotropic media," *Journal of the Optical Society of America A*, Vol. 18, No. 11, 2886–2894, 2001.

[80] Popov, E., "Differential method for periodic structures," in *Gratings: Theory and Numeric Applications, Second Revisited Edition*, 7.1–7.57, E. Popov (ed.), AMU (PUP), Apr. 2014.

[81] Schuster, T., J. Ruoff, N. Kerwien, S. Rafler, and W. Osten, "Normal vector method for convergence improvement using the RCWA for crossed gratings," *Journal of the Optical Society of America A*, Vol. 24, No. 9, 2880–2890, 2007.

[82] Martí, R., "Multi-start methods," in *Handbook of Metaheuristics*, 355–368, F. Glover and G. A. Kochenberger (eds.), Springer US, Boston, MA, 2003.

[83] Ugray, Z., L. Lasdon, J. Plummer, F. Glover, J. Kelly, and R. Martí, "Scatter search and local NLP solvers: A multistart framework for global optimization," *INFORMS Journal on Computing*, Vol. 19, No. 3, 313–484, 2007.

[84] The MathWorks, Inc., "Matlab R2019a and Optimization Toolbox 8.3," Natick, MA, USA, 2019.